Faculteit Industriële Ingenieurswetenschappen

master in de industriële wetenschappen: bouwkunde

Masterthesis

Out-of-plane two-way bending shaking table tests on gable walls

Jolien Habraken
Nick Smeets

Scriptie ingediend tot het behalen van de graad van master in de industriële wetenschappen: bouwkunde

PROMOTOR :
Prof. dr. ir. Herve DEGEE

PROMOTOR :
Prof. Francesco GRAZIOTTI

Gezamenlijke opleiding UHasselt en KU Leuven

UHASSELT KU LEUVEN

Universiteit Hasselt | Campus Diepenbeek | Faculteit Industriële Ingenieurswetenschappen | Agoralaan Gebouw H - Gebouw B | BE 3590 Diepenbeek

Universiteit Hasselt | Campus Diepenbeek | Agoralaan Gebouw D | BE 3590 Diepenbeek
Universiteit Hasselt | Campus Hasselt | Martelarenlaan 42 | BE 3500 Hasselt

UHASSELT KU LEUVEN

2023
2024

Faculteit Industriële Ingenieurswetenschappen

master in de industriële wetenschappen: bouwkunde

Masterthesis

Out-of-plane two-way bending shaking table tests on gable walls

Jolien Habraken
Nick Smeets

Scriptie ingediend tot het behalen van de graad van master in de industriële wetenschappen: bouwkunde

PROMOTOR :

Prof. dr. ir. Herve DEGEE

PROMOTOR :

Prof. Francesco GRAZIOTTI

UHASSELT KU LEUVEN

Foreword

This thesis marks the culmination of our studies in the field of structural and earthquake engineering, specifically focusing on the impact of earthquakes on masonry gable walls. The opportunity to provide research on this topic was given by the university of Pavia after the decision to go abroad, which extended our knowledge and interests in seismic engineering.

This thesis is a collaborative effort between the two of us. Over the past half year, we have worked closely together, combining our insights to investigate the seismic behaviour of gable walls. The division of work was based on our individual strengths and interests, helping us to handle different parts of the research effectively.

We would like to express our gratitude to our supervisors, Professor F. Graziotti at the University of Pavia and Professor H. Degee at Hasselt University, for their guidance and support throughout this project. Their expertise and encouragement have been instrumental in shaping our research.

We would also like to thank Satyadhrik Sharma for his guidance and assistance during the experiments. Our appreciation also extends to our fellow students, Marco Smerilli and Marta Bertassi for the good cooperation, the constructive feedback and support provided by colleagues, as well as the contributions of the laboratory members in assisting with the experiments, are gratefully acknowledged.

Studying as Erasmus students at the University of Pavia in Italy has been an enriching experience. The different academic environment and the opportunity to collaborate internationally have broadened our perspectives and enhanced our research.

Finally, we hope that this thesis helps the understanding of seismic effects on gable walls consisting of masonry with out-of-plane behaviour and serves as a foundation for future research in this field.

Table of contents

List of tables

List of figures

Glossary

- AOI

The Area of Interest refers to the specific region on the surface of a specimen where displacement, strain or deformation is measured and analysed.

- C.o.V.

The coefficient of variation quantifies relative variability by calculating the ratio of the standard deviation to the mean.

- DIC

Digital Image Correlation is an optical measurement method used to analyse surface deformation, displacement and strain by comparing images of an object taken before and after deformation.

- Doublets

A doublet is a test specimen composed of two bricks, designed to simulate a section of a masonry wall for experimental research.

- FPS

Frames per second is the rate at which consecutive frames are captured

- LVDT

A Linear Variable Differential Transformer is an electromechanical sensor that measures linear displacement.

- Triplets

A triplet is a test specimen composed of three bricks, designed to simulate a section of a masonry wall for experimental research.

- Wallets

A wallet is a small wall segment made of bricks and mortar, used to evaluate the mechanical properties under various load conditions.

Abstract

Unreinforced masonry (URM) walls with triangular gables are common in seismically active areas and are highly vulnerable, particularly at the gables. This due to factors like high slenderness, poor roof connections and amplified seismic forces with minimal additional load. Flexible roof diaphragms worsen the issue. However, experimental data on URM gables is limited and usually comes from tests on entire buildings rather than focused studies on the gable themselves.

Recent seismic events have highlighted the importance of out-of-plane (OOP) mechanisms in the collapse of unreinforced masonry (URM) buildings. These failures occur more often due to displacement beyond equilibrium within the kinematic chain, rather than stress capacity being exceeded. Despite being a frequently reported and surveyed cause of structural damage, scarce research has been directed towards the OOP failure mechanism in gable walls. To address this gap, a research initiative was launched at EUCENTRE Pavia, in collaboration with the University of Pavia, Delft University of Technology (TU Delft) and the Netherlands Organisation for Applied Research (TNO), focusing on gable walls.

This experimental attempt aims to address the existing knowledge gap by conducting dynamic testing on three full-scale gables consisting out of replicated historic masonry. Each full-scale specimen consists of an out-of-plane (OOP) panel with same conditions but applied with different loads at the top table and same loads at the bottom table. The various loads at the top table simulate the different roof configurations of stiff, semi-flexible and flexible case that the gable could support. These specimens were subjected to incremental input motions until collapse occurred.

The experimental results are analysed and presented in terms of deformation of the configurations, failure mechanisms, force-displacement curves, aiming to clarify the dynamic behaviour of these structural configurations. A study was also conducted using the virtual work method (VWM) to calculate predictions of the gable's behaviour. Furthermore, a thorough mechanical characterization of all materials employed in these specimens is provided. It was found afterwards that the tested gables did not exhibit the predicted two-way bending but instead showed one-way bending out-of-plane behaviour.

Additionally, a comprehensive study was carried out in the shear behaviour between the mortar and the brick, focusing on triplets with the same construction assembly as the tested facades. These triplets were tested and analysed using the DIC program to determine whether the DIC program is as accurate as the measurement equipment currently used to determine displacement during the test. The results indicate that the DIC program is accurate, which should be further refined in the future.

1 Introduction

Research on the seismic vulnerability of gable walls, particularly those in the context of seismic activity specific to Groningen, is limited. The gable wall is a critical component of a structure, particularly in historical buildings, as it is highly susceptible to collapse during earthquakes. Recognizing this vulnerability, especially in the context of fracking-induced seismic events in Groningen, TU Delft collaborated with the EU Centre to gain a deeper understanding of the associated risks. This partnership aimed to address the research gap and enhance the safety of buildings in the region.

The seismic resistance of one-way spanning unreinforced masonry (URM) walls, including gables, primarily relies on their geometric stability. The slender nature of these elements and the low tensile strength of masonry can trigger a rocking failure mechanism under moderate seismic loading conditions. Consequently, force-based static predictions of gable capacity tend to be overly conservative. Furthermore, the static instability displacement of these elements often differs significantly from their dynamic instability threshold and clear correlation between the two has yet to be established.

The out-of-plane (OOP) behaviour of URM walls remains a complex and poorly understood aspect of structural seismic analysis. This complexity arises from factors such as the anisotropic nature of masonry, the structural indeterminacy of wall configurations, and the presence of internal flexural stresses acting in multiple directions. Post-earthquake observations and experimental outcomes have highlighted the significant vulnerability of URM gables to overturning mechanisms, both because of inertial OOP excitation and the in-plane deformability of timber diaphragms. Roof structures and gable walls are among the most critical vulnerabilities in URM structures under seismic loading, with collapses often occurring due to insufficient connections between the gable wall and the roof diaphragm or between the gable wall and transverse walls.

To provide realistic results dynamic experiments conducted on shake tables are essential to quantify the displacement capacity of URM gables and account for potential dynamic equilibrium under seismic acceleration. Moreover, the interaction between gables and the connected timber roof structure significantly influences the dynamic response of the gable. The testing facilities available at the EUCENTRE enable the application of different motions at multiple vertical levels, providing a unique opportunity to conduct dynamic experiments while considering varying stiffness values for the roof and its impact on gable performance.

The proposed project aims to enhance understanding of the seismic response of masonry gables in existing buildings. The purpose of this research is to generate new experimental data on the dynamic behaviour of URM gables, addressing in

current gap in the literature. The experiments employ simplified and easily replicable boundary conditions, facilitating numerical simulations. These tests will serve as benchmarks for refining existing numerical models and developing new tools, including those based on single-degree-of-freedom systems.

Given the limited experimental data specifically focused on gables, current assessment guidelines often rely on correlations between static instability displacement and the dynamic point of instability derived from studies on one-way spanning walls with rectangular geometry. This approach is often extended to gables with triangular geometry as well.
This research involves conducting incremental dynamic tests on three full-scale brick masonry gables. The interaction with the roof is simulated by adjusting the input motions at the bottom and top platforms. The tests encompass various typologies of roof diagrams to examine their impact on the gables' behaviour. Companion material characterization tests are conducted to understand the behaviour of the masonry and connections.

The simulation on the shake table is intended to replicate the conditions of a terraced house located in the Groningen region of the North-East Netherlands. Most existing buildings in the region are low-rise unreinforced masonry (URM) structures, which were not originally designed to withstand seismic loads. Earthquakes in this region are typically shallow and induced by gas extraction, characterized by lower amplitude ground motions. After simulating the Groningen scenario, the experiment will proceed with higher seismic intensities to simulate conditions associated with more severe earthquakes.

2 Material characterization tests

Prior to subjecting the specimens to shake table testing, comprehensive material characterization of both the individual components, brick units and mortar, as well as the masonry as a composite material was conducted. This characterization is critical for understanding the strength, durability, and overall behaviour of the masonry under seismic loading, thereby ensuring accurate interpretation of the shake table results and informing the design of resilient structures. To achieve these objectives, the following tests were conducted:

- The flexural (f_t) and compressive strength (f_c) of the mortar were determined following the recommendation of EN 1015-11 (1999) [1].
- The compressive (f_b) and flexural tensile strength (f_{bt}) of the units were established according to the guidelines outlined in EN 772-1(2011) [2] and EN 6790 (2005) [3], respectively.
- The initial shear strength (f_{v0}) and friction coefficient (μ) were conducted by subjecting masonry triplets to translational shear tests according to the guidelines outlined in EN 1052-3 (1998) [4].
- In addition to conventional shear tests, torsional shear tests will be conducted on masonry doublets featuring a reduced bedded area, representative of the overlap between adjacent bricks in two successive layers within a wall. This approach enabled the determination of both the initial torsional shear strength ($f_{v0,\tau}$) and the friction coefficient (μ_τ). Notable, no existing guidelines for conducting these tests were found to be followed.
- To identify the bond strength of masonry (f_w) the bond wrench test was conducted on masonry doublets according to EN 1052-5 (1998) [5].

A comprehensive description of each characterization test is provided in following subsections. Summaries of the material properties are outlined in Table 1 : Summary properties [6].

Table 1 : Summary properties masonry and its components

Material properties	*Symbol*	*UM*	*Specimens*	
			Mean	*C.o.V. (%)*
Density of the masonry	ρ	[kg/m3]	2000	-
Compressive strength of the mortar	f_c	[MPa]	0.71	14
Flexural strength of the mortar	f_t	[MPa]	0.20	40
Compressive strength of the brick	f_b	[MPa]	42.57	8.6
Compressive strength of masonry perpendicular to bed joints	f_m	[MPa]	7.44	10

Elastic modulus of masonry in the direction perpendicular to bed joints (10-33%)	E_m	[MPa]	4072	11.2
Elastic modulus of masonry in the direction perpendicular to bed joints (0-10%)	E_m	[MPa]	6032	34
Elastic modulus of masonry in the direction perpendicular to bed joints (0-33%)	E_m	[MPa]	4445	14.6
Masonry (bed joint) initial shear strength (direct)	f_{v0}	[MPa]	0.2127	-
Masonry (bed joint) shear friction coefficient (direct)	μ	[-]	0.7428	-
Masonry (bed joint) initial shear strength (torsional)	$f_{vo,tor}$	[MPa]	-	-
Masonry (bed joint) shear friction coefficient (torsional)	μ_{tor}	[-]	-	-
Bond wrench strength	f_w	[MPa]	0.21	33

These material properties are applicable to all specimen tested, as the same façade properties are being tested but under different conditions.

2.1 Mortar characterization tests

The mortar characterization tests were provided to obtain the compressive and flexural tensile strength of the mortar. These tests were conducted conform with the European norm EN 1015-11 [1].

The mortar specimens are dimensioned by 160x40x40 mm corresponding to the dimensions of the mould, used to cast the samples as shown in Figure 1. These specimens have had a drying period of 2-3 days in the mould until they could be demoulded, as illustrated in Figure 2 and Figure 3.

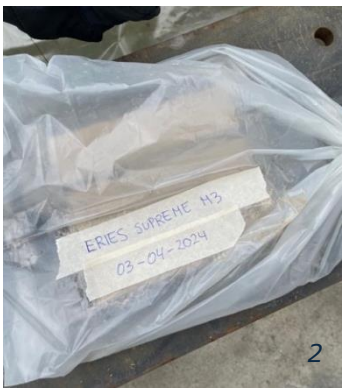

Figure 1 : Making the specimens in the mould
Figure 2 : Specimens covered to keep them moist
Figure 3 : Cured mortar specimens

After demoulding, the specimens were covered with plastic to keep them in a moist environment and prevented from cracking. Thereafter they are left to dry in a mortar conditioning chamber at a constant temperature of 20°C. Upon completion of the prescribed 28-day curing period, the specimens are ready for comprehensive testing.

The type of mortar used to construct the gable is grade MM 3 mortar with a mean compressive strength equal to 3 MPa. This type was selected to resemble the characteristics of historical masonry, which has reduced strength due to the effects of degradation over time. However, it was initially expected that the chosen mortar type would be stronger than the predetermined expectations. For this reason, standardized tests were performed on each new test specimen of the mortar made for the gables.

The mortar samples utilized were poured during the construction of the masonry specimens. This procedure was executed to facilitate the characterization of mortar within the masonry specimens under review. Moreover, mortar samples were poured twice a day throughout the construction process of the specimens and walls. Specially, three cuboids of mortar were casted in both the morning and the afternoon to capture samples representative of various stages of the construction of each masonry specimen.

2.1.1 Flexural tensile strength f_t of the mortar specimens

Mortar, like other brittle materials, is generally weak in tension. Flexural tensile strength tests provide a measure of the mortar's ability to resist bending and cracking. Mortars with higher flexural tensile strength are less likely to crack under tensile stress, thereby enhancing the durability and longevity of the structure.

Each mould provides three test samples for assessing flexural tension. Initially, the flexural tensile strength of each mortar specimen was assessed using a three-point bending test. The specimens were positioned between two rollers, connected to the testing machine with a distance of respectively 20 mm from the nearer edge of the mortar specimen as shown in figure 4.

The compressive machine is operated with a constant loading rate, falling of between 50-100 N/s, ensuring that failure occurs within the timeframe of 30 to 90 seconds. The flexural test resulted in two fractured parts of the mortar parallelepiped, illustrated in figure 5 [6].

Figure 4 : Test setup determination of flexural strength

Figure 5 : Failure crack of the mortar

The flexural tensile strength (f_t) of the mortar specimens was calculated using the following formula:

$$f_t = 1.5\frac{F \cdot l}{b \cdot d^2} \text{ [MPa]} \qquad [1]$$

where F = the maximum load applied to the specimen [N];
l = the distance between the rollers = 120mm [mm];
b = the width of the specimen [mm];
d = the thickness of the specimen [mm].

2.1.2 Compressive strength f_c of the mortar specimens

Compressive strength is the most critical mechanical property of mortar, given that masonry structures are predominantly subjected to compressive loads. The assessment of compressive strength is conducted immediately following the flexural test, the mortar specimens were split in half allowing both sides to be utilized resulting in 6 samples per mould show, by applying a load until failure. Subsequently, an increasing force is gradually and smoothly applied to induce failure of the specimen, these specimens are illustrated in Figure 6.

Figure 6 : compressive strength specimens after testing flexural strength
Figure 7 : setup compressive strength of the mortar
Figure 8 : Failure mortar under compressive strength

During the compressive test, the samples are positioned centrally on the pressure surface, shown in Figure 7. It is crucial to ensure that the surfaces are smooth and in complete contact with the plate to ensure even distribution of force. The loading

speed is set to 0.4 kN/s, gradually increasing the applied force until failure represented in Figure 8, while avoiding any sudden shocks [6].

The compressive strength (f_c) of the mortar specimens was evaluated using the following formula:

$$f_c = \frac{F_c}{A_c} \text{ [MPa]} \qquad [2]$$

where F_c = the maximum compressive force applied to the specimen at the moment of failure [N];
A_c = the contact area of the specimen with the plates of the machine test [mm²].

The mean flexural and compressive strengths of mortar utilized are summarized in Table 2.

Table 2 : Mean compressive and flexural strength of the mortar

	Gable 1		***Gable 2***		***Gable 3***	
	f_c	f_t	f_c	f_t	f_c	f_t
	[MPa]	[MPa]	[MPa]	[MPa]	[MPa]	[MPa]
Mean	0.64	0.19	0.89	0.23	0.59	0.18
St.dev.	0.09	0.12	0.15	0.06	0.07	0.05
C.o.V.	14.06%	63.16%	16.85%	26.09%	11.86%	27.78%

2.2 Bricks characterization tests

In a similar way to the mortar tests, the compressive strength and flexural strength of the brick units were determined. The bricks used for this research are the standard fired clay Italian bricks dimensioned by 105x55x230 mm.

2.2.1 Compressive Strength f_b of the bricks

The compressive strength of the bricks used was evaluated according to the guidelines of EN 772-1(2011) [2]. The bricks were positioned with the surface of 105x230 mm on the compression machine's plate to compute the strength in the direction of the weak axis, shown in Figure 9. The load was gradually increased from zero until the brick failed, as shown in Figure 10. To compute the compressive strength, six samples were tested to gain an overall view, these are shown in figure 11. [6]

Figure 9 : Test setup of compressive strength of unit

Figure 10 : Failure of the unit

The mean compressive strengths of the bricks utilized are summarized in Table 3 These values reflect the uniformity and quality of the bricks produced. A high coefficient of variation (C.o.V) in compressive strength may indicate potential deficiencies in the material. The results also demonstrate that the bricks meet the specified design requirements, as outlined in the technical specifications.

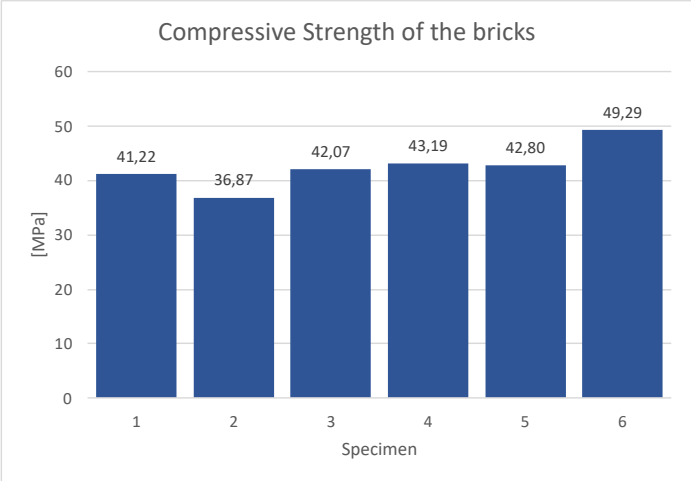

Figure 11 : Distribution of compressive strength of the brick units

Table 3 : Mean compressive and flexural strength of the brick

	f_b
	[MPa]
Mean	42.57
St.dev.	3.66
C.o.V.	8.59%

2.3 Masonry characterization tests

The masonry test evaluates the interaction between bricks and mortar as an integrated system. It considers the impact of factors such as mortar thickness, bond quality, and potential voids, which can affect the overall strength and stability of the masonry.

2.3.1 Compressive Strength f_m of the masonry

The compressive behaviour of the masonry in a direction perpendicular to the bed joints was assessed following the recommendations of EN 1052-1(2011) [2]. These tests allowed for the determination of the masonry's compressive strength (f_m) as well as the secant modulus of elasticity at 10% and 33% of the compressive strength (E_1).

According to these guidelines, at least three walls conforming to the specified geometrical configurations are required to be tested for compressive strength as described above. In contrast, six walls were tested for compressive strength. The mortar and bricks used are described in the previous paragraph. Schematic diagrams of these wallets can be seen in Figure 12 [6].

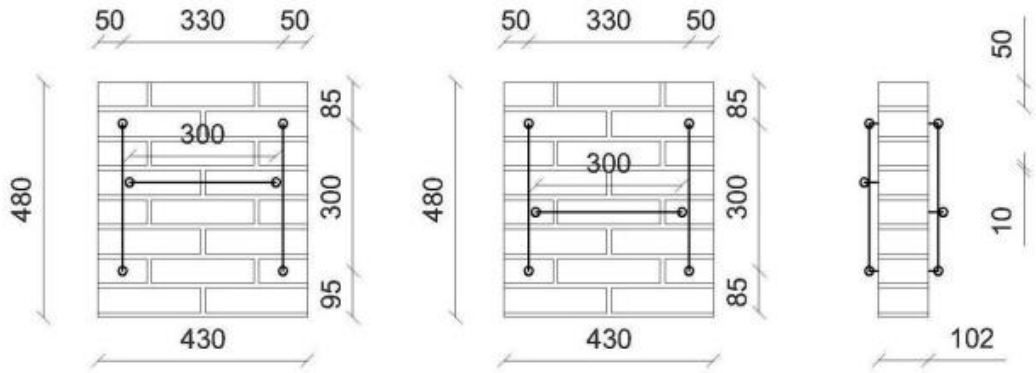

Figure 12 : Schematic of adopted instruments on the masonry walls tested in compression

Each specimen was equipped with three potentiometers, two vertical and one horizontal, on each side of the wall. The horizontal potentiometer was positioned at mid-height of the fourth layer of bricks. The same setup was used on the back side, except that the horizontal potentiometer was placed at the mid-height of the fifth layer. An illustration of the instrumentation used for the masonry can be seen in Figure 13 and figure 14. It is also crucial to ensure uniform stress distribution and eliminate any loading eccentricities caused by imperfections in the geometry. To achieve this, layer of gypsum is applied to the top and bottom surfaces of the wallettes.

Figure 13 : Instrumented wall, front side

Figure 14 : Instrumented wall, back side

Figure 15 : Failure wall after compression, front side

Figure 16 : Failure wall after compression, side

The loading protocol comprised three sequential steps, each involving a series of three uniform cycles of loading and unloading at a consistent velocity. The initial cycle continued until a load of 8.5 kN was reached, followed by the second cycle up to 12.0 kN, and finally a third cycle with a maximum load of 17 kN, shown in Figure 17. Upon completion of these stages, the load was incrementally increased until the specimens failed under vertical compression loading, shown in [6].

The loading cycle, as seen on Figure 17, performed manually, adhering to the velocity parameters specified in EN 1052-1(1998) [7]. This procedure resulted in an approximate test duration of around two hours for each wallette. The calculation of the elastic modulus of masonry in addition to determining its compressive strength was derived.

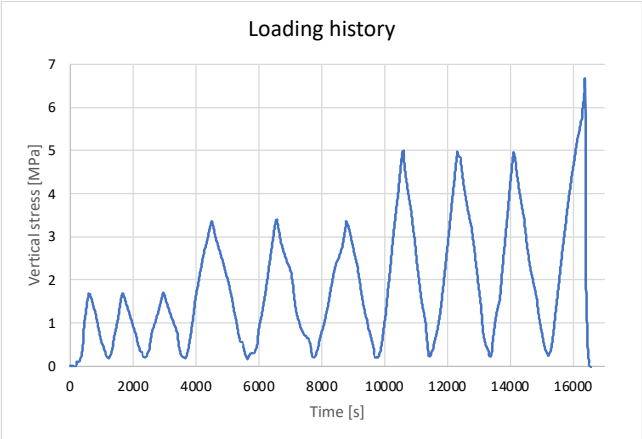

Figure 17 : Loading history, vertical stress vs. time, for compression testing of the wallettes

The compressive strength (f_m) of the masonry walls was evaluated using the following formula:

$$f_m = \frac{F_{max}}{A} \text{ [MPa]} \qquad [3]$$

where F_{max} = the maximum force the walls resisted [N];
A = the specimen's contact area with the machine plates [mm²].

The compressive strength results for all tested wallettes are summarized in

Table 4. Vertical and horizontal deformations/strains were computed by averaging the deformations/strains recorded by each vertical and horizontal potentiometer in the same directions. It is worth noting that E_1 is calculated as the secant elastic modulus between 10% and 33% of f_m and the origin (0;0) from a graph depicting vertical stress and vertical strain. The distribution of compressive strengths and secant modulus can be observed in figure 18, figure 19, figure 20 and figure 21 respectively.

Table 4 : Compressive strength and elastic moduli of the masonry wallettes

$No.$	f_m	$E_1(10-33\%\ f_m)$	$E_1(0-33\%\ f_m)$
	[MPa]	*[MPa]*	*[MPa]*
1	7.43	3271	3198
2	7.71	4518	4470
3	8.74	3863	4606
4	7.18	4125	4565
5	6.89	4209	4719
6	6.66	4448	5113
Mean	7.44	4072	4445
St.dev.	0.74	458	651
C.o.V.	9.96%	11.24%	14.64

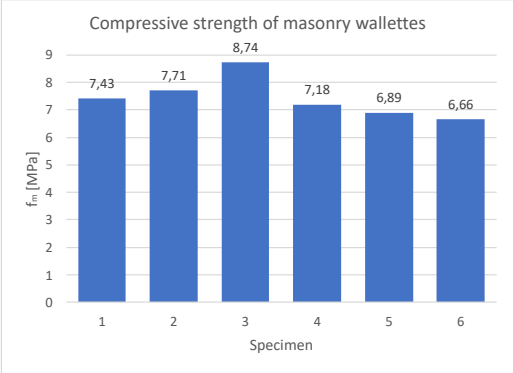

Figure 18 : Compressive strength of masonry wallettes

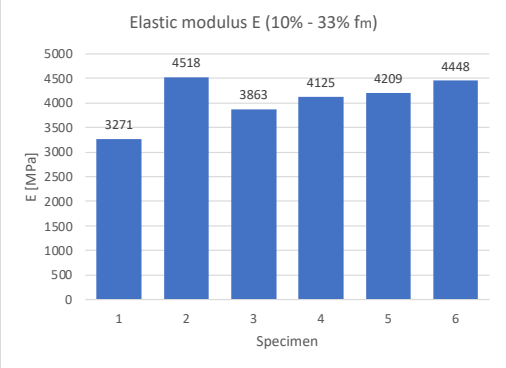

Figure 19 Elastic modulus E (10% - 33% f_m)

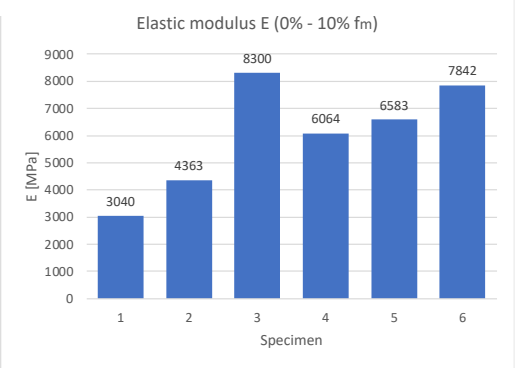

Figure 20 Elastic modulus E (0% - 10% f_m)

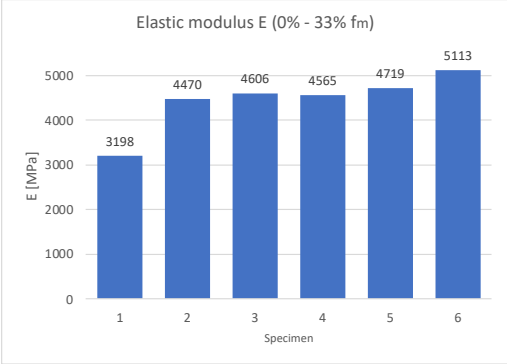

Figure 21 Elastic modulus E (0% - 33% f_m)

2.3.2 Determination of Bond Strength f_w

Bond strength quantifies the effectiveness of the bond between bricks and mortar, which is crucial for ensuring proper adhesion of the mortar to the masonry units. Testing bond strength can uncover potential issues with the materials used, such as deficiencies in the mortar mix or application techniques.

To establish the bond strength of the horizontal bed-joints, the bond wrench test was accomplished. These tests were performed to evaluate the strength of the masonry joints following the provision of NEN 1052-5 [5] [6].

The tests were conducted on masonry doublets consisting of two bricks bonded together with a mortar bed-joint, positioned on a horizontal surface.

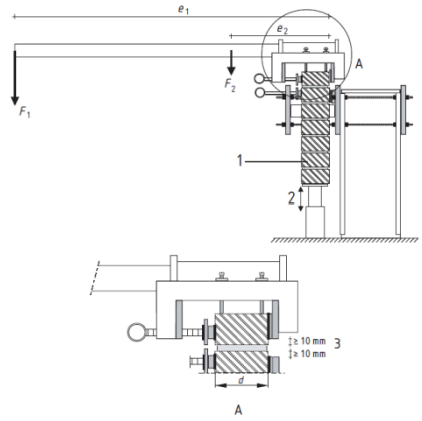

Figure 22 : Schematic of the test setup of the bond wrench test

Figure 23 : Failure of the bed joint 1

Figure 24 : Failure of the bed joint 2

The lower brick was securely clamped, thereby isolating the test to solely the top bed joint. To the upper brick a torque wrench was fixed. Subsequently, a bending moment ($M = F_1 * e_1$) was applied to the clamp by a lever until the upper brick separated from the specimen, as presented in Figure 23 and Figure 24. Through the analysis of the stresses incurred by the specimen, the bond strength of the masonry can be assessed.

Figure 22 illustrates the specified parameters for the test setup. The parameters for the conducted test are as follows: F_2= 75 N, e_1= 530 mm, e_2= 210 mm, d = 105 mm. Figure 25 illustrates the potential failure modes that can be occurred within the bed joint.

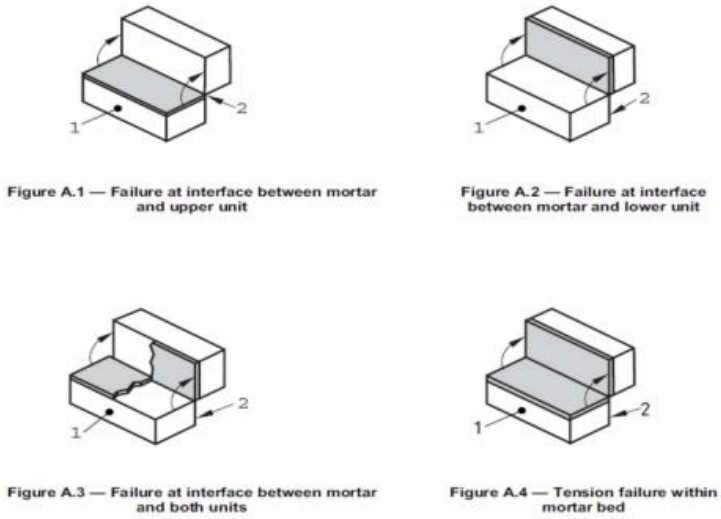

Figure 25 : Modes of failure of the bed joints for the bond wrench test in accordance with EN 1052-5 [5]

The bond wrench strength (f_w) corresponding with the bed joints were evaluated using the following formula:

$$f_w = \frac{F_1 \cdot e_1 + F_2 \cdot e_2 - \frac{2}{3} d \cdot \left(F_1 + F_2 + \frac{W}{4}\right)}{Z} \text{ [MPa]} \qquad [4]$$

where

F_1 = failure load obatianed with torque wrench moment [N];
F_2 = normale force as a result of the weight of the bond wrench device [N];
e_1 = distance from the applied load to the centre the specimen [mm];
e_2 = distance from the device's centre of mass to the specimen's centre [mm];
W = weight of the masonry and the adherent mortar [g];
Z = the section modulus of the failure surface [mm³];
d = the mean depth of the specimen [mm].

The bond wrench tests are summarized in Table 5 , along with the associated failure mode according NEN-EN 1052-5, shown in Figure 25 [5].

Table 5 : Summary of results from the bond wrench test of the masonry

	Gable 1	***Gable 2***	***Gable 3***
	f_{wi}	f_{wi}	f_{wi}
	[MPa]	*[MPa]*	*[MPa]*
Mean	0.24	0.28	0.11
St.dev.	0.13	0.10	0.02
C.o.V.	54.17%	35.71%	13.63%

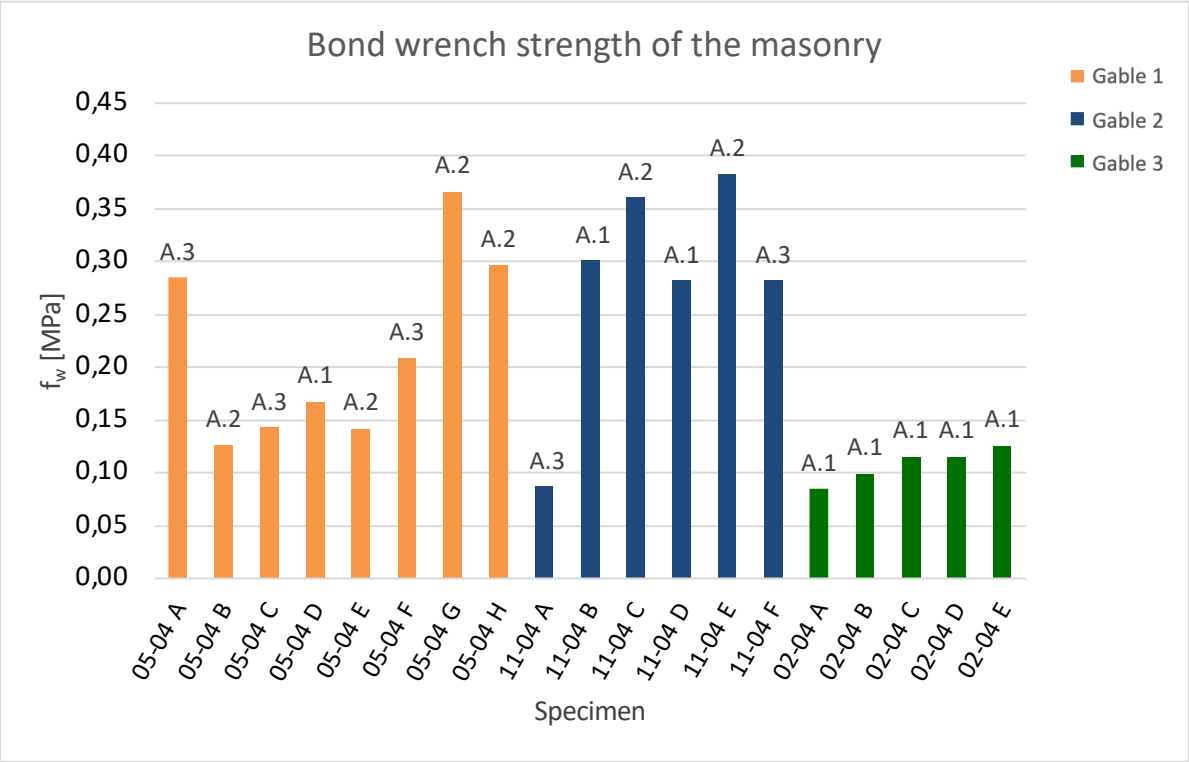

Figure 26 : Distribution of bond wrench strength along with associated failure mode of the masonry

Due to the variable strength observed in the bond wrench test samples, additional samples were collected after the completion of the gable tests to facilitate a comparison between the characterization tests and the masonry utilized in the gable. This approach yielded more consistent data. The wall was subjected to its own weight, which induced precompression during the hardening process. In contrast, the doublets were not exposed to any external forces during their hardening phase.

2.3.3 Determination of Shear Strength f_{v1} (Translational)

In accordance with the recommendations outlined in EN 1052-3 (1998) [4] and EN 1052-3/A1:2007 [8], the study adhered to the requirements of EN 1052-3:2002 [9], which necessitates testing a minimum of at least nine triplets. Direct shear tests were conducted on clay masonry triplets, each consisting of three units and two bed joints [6].

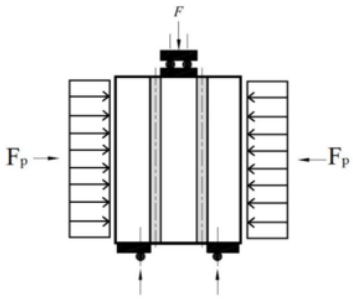

27

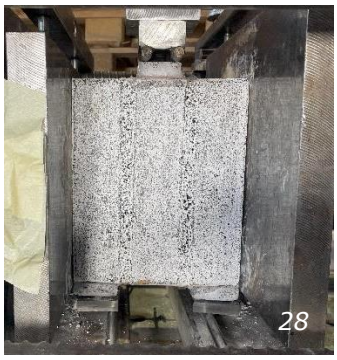

28

29

Figure 27 : Applied loads during shear tests conducted on triplets
Figure 28 : DIC instrumentation adopted to determine the shear strength, front side
Figure 29 : DIC instrumentation adopted to determine the shear strength, back side

Determining the initial shear strength of masonry bed joints involves measuring the strength and observing the post-peak behaviour. This process allows for the calculation of cohesion (f_{v0}) and friction coefficient (μ).

The specimens are outfitted with one horizontal and two vertical potentiometers on both the front and back faces of the triplet. Additionally, a small plate fixed to the central brick measures the displacements of the outer bricks relative to the central block.

To ensure the uniform application of the precompression load, a layer of gypsum was applied on the exteriors of the bricks. The specimen was then rotated 90 degrees from the laying plane of the bricks accommodating the operational requirements of the testing machine in the laboratory. The specimen was positioned within the test setup between two steel plates. Additionally, two rollers were positioned beneath the outer two bricks to provide support and ensure the application of a point load rather than a distributed load.

A pre-compression load, F_p , was applied to the specimen using a vertical actuator in series with a spring. In accordance with the EN 1052-3 [4] standards, units with a compressive strength exceeding 10 MPa, in this case, must be subjected to three distinct levels of F_p. These result in pre-compression stresses of 0.2 MPa, 0.6 MPa and 1.0 MPa phases of the test. The series spring facilitated the accommodation of dilatancy and was calibrated to have a spring constant of 150 N/mm [6].

Figure 27 : test set-up used for shear strength

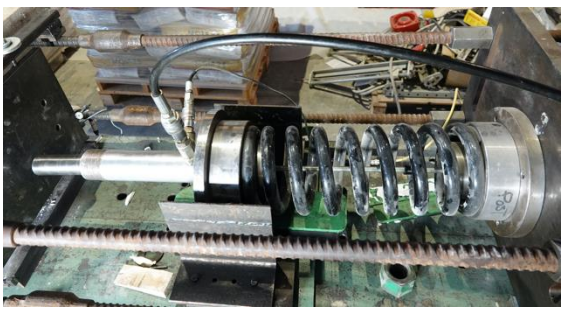

Figure 28 : Spring loaded vertical actuator

The shear force F was applied by an actuator operating in displacement control, perpendicular to the central brick, using two rollers positioned on the inner brick. This setup adhered to the EN 1052-3 [4] standard, specifically regarding the distance of the rollers from the bed joints. The load was applied at a rate of 0.02 mm/sec, which is within the EN 1052-3 [4] specifications that restrict the rate to between 0.1 MPa/min and 0.4 MPa/min and was increased progressively until failure occurred [6].

For each specimen, the pre-compression stress (f_p) and the shearing stress (f_v), at the moment of bed joint failure, were computed using the following formulas:

$$f_{pi} = \frac{F_{pi}}{A_{ei}} \quad \text{[MPa]} \qquad [5]$$

$$f_{vi} = \frac{F_{i,max}}{2 \cdot A_{ei}} \quad \text{[MPa]} \qquad [6]$$

where F_{pi} = the pre-compression force [N];
A_{ei} = the effective area of contact [mm²];
$F_{i,max}$ = the shear failure force [N].

Each specimen was characterized by a pair of values f_{pi} and f_{vi}. These values were plotted to derive a representation of Coulomb's friction law. In this representation, the shear strength of masonry triplets f_v is influenced by three parameters: cohesion, the coefficient of friction, and transverse compression. Cohesion affects the shear strength only when the bedding mortar remains intact, whereas frictional forces continue to contribute to shear strength post-cracking, provided there is ongoing contact between the materials. Consequently, the shear strength f_v of the masonry, according to Coulomb's friction law, which linearly depends on the pre-compression stress f_p, can be mathematically expressed as:

$$f_v = f_{v0} + \mu \cdot f_p \quad \text{[MPa]} \qquad [7]$$

where f_{v0} = the cohesion [MPa];
μ = the friction coefficient.

The cohesion and internal friction angle were determined from the results presented in Table 6. It is important to note that the residual shear strength of the bed joint, obtained by continuing the test beyond the failure point if the bed joint, were used to validate the friction coefficient derived from the Coulomb's law representation of these results, as shown in Figure 29 [6].

Table 6 : Summary of results of direct shear testing of masonry triplets

	f_{pi}	f_{vi}
Triplet No.	*[MPa]*	*[MPa]*
1	0.183378	0.091226
2	0.233756	0.176851
3	0.543974	0.386304
4	0.426671	0.068789

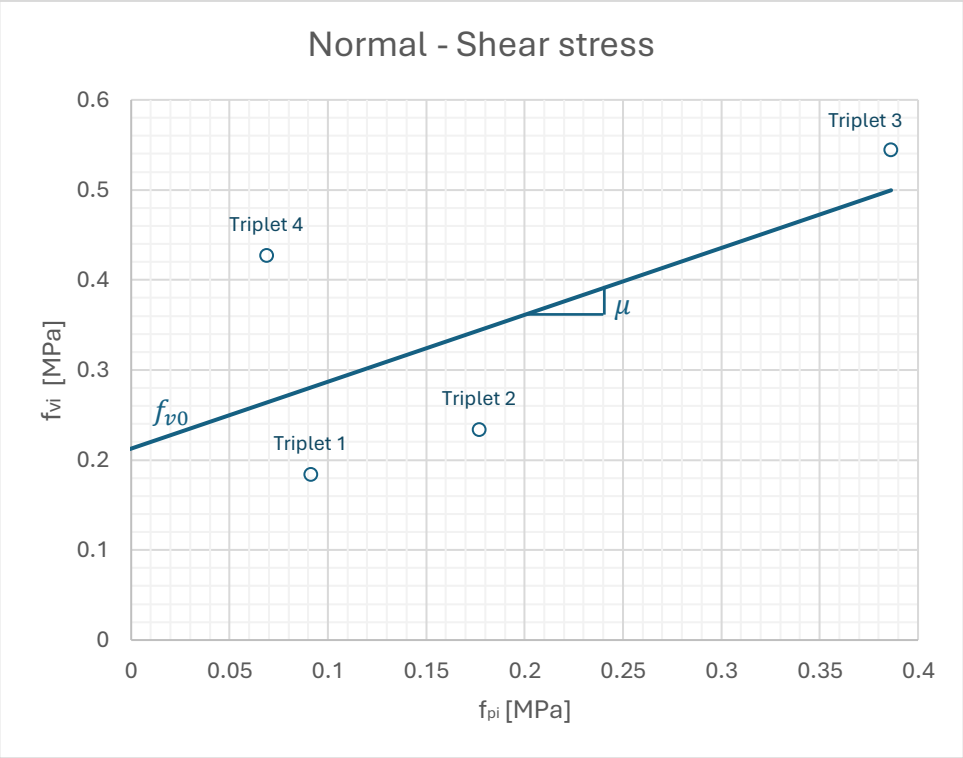

Figure 29 : Coulomb's friction law representation of results of the triplets in direct shear

3 Digital image correlation (DIC) on shear strength test (Translational)

3.1 Shear strength test setup utilizing the DIC method

During the previously described shear strength test on the triplets. Displacement transducers were used to measure the displacement of the specimen relative to a fixed point. These instruments provide time data corresponding to the resulting crack pattern. This study investigates the application of the DIC method to the crack pattern present in the bed joint of a masonry test specimen during the shear strength test. The Digital Image Correlation (DIC) technique is utilized to monitor the crack patterns and wall displacement throughout different phases on the test using picture frames taken during the test. The key aspects include advanced techniques for point tracking and accurate correlation, enabling detailed analysis of material behaviour under stress. The comparison can be done by performing various tests where the instruments are attached to the specimen and the DIC method is applied simultaneously, with results compared afterwards.

3.1.1 Linear variable differential transformers (LVDTs)

Three LVDTs were used to measure the displacement in the test specimen, the triplets, during the experiment. Two LVDTs were positioned vertically on the back side of the specimen to measure in-plane displacement at different positions, referred to as POT_0 and POT_1 from left to right. Additionally, a horizontal LVDT, referred to as POT_2, was installed to monitor horizontal expansion. Figure 31 shows the location of these displacement transducers.

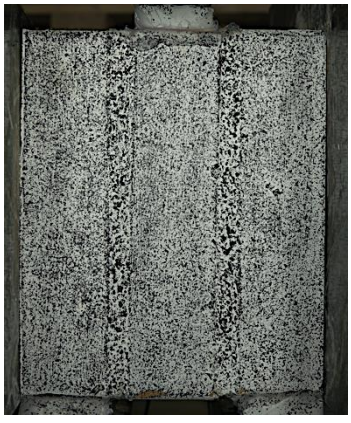

Figure 30 : Speckle pattern on triplet

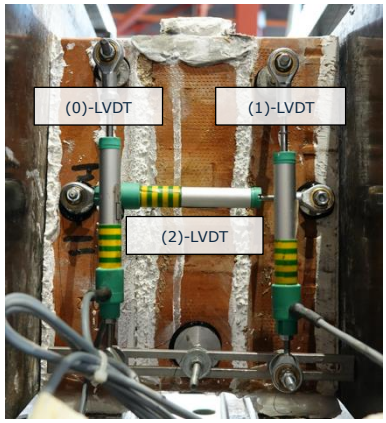

Figure 31 : Instrumentation adopted for shear test triplets

3.1.2 Surface preparation and speckle pattern application

To obtain accurate results in the DIC software, the surface of the specimen must be properly prepared. For these tests, a white primer was first applied to the samples, followed by the application of a random black speckle pattern. The DIC software tracks these speckles in detail by utilizing the contrast between the black and white paint, see Figure 30. Different methods to apply a stochastic pattern were tested on pieces of paper. The pattern with the best pattern quality in ZEISS was selected.

3.1.3 Camera set-up for the DIC method

The DIC software used in this study is Zeiss INSPECT Correlate. This software provides full-field 2D displacement and strain data using optimized correlation algorithms, allowing for the measurement of in-plane displacements at every pixel subset within the specified area [10]. Photographs were taken at required intervals to enable the DIC software to track cracks and joint openings during the tests. The camera, Sony RX10 IV, was set on a timer to automatically capture images every 1/16 seconds during the wallette testing. Short-distance lighting was employed to ensure uniform, bright illumination on the triplet, which is necessary to obtain high-quality images for DIC analysis. To reduce the amount of blur in an image, the right settings were conducted, the camera settings were as follows: manual mode, ISO 640, shutter speed 1/80, and aperture F3.5.

3.1.4 Cyclic in-plane loading protocol and vertical pre-compression loading

During the test, a hydraulic press was positioned vertically against the wallette to apply a specific compressive force. The vertical load was equivalent to i.e. 0.1, 0.2 and 0.4 MPa as per the EN 1052-3 [8], resulting in increasing load on the Wallette until the resistance of the mortar was reached. The displacement time history adopted for this study was based on a static cyclic displacement time history (frequency = 256 Hz). Lateral displacements were incrementally applied in computer-controlled steps, with each step utilizing an increasing target displacement rate.

High-resolution photographs were captured during the test as the applied load increased. The images were taken at various stages with an approximate time interval of 1/9 seconds between each photo. This includes a pre-loading state and several post-loading states to capture the relative movement of the speckle pattern in relation to the wall deformation. The photographs are then processed using Zeiss INSPECT Correlate software [10] to determine the full-field displacement and strain of the specimen [11] [12].

3.2 Digital image correlation (DIC) method

The Digital Image Correlation (DIC) method is a straightforward and detailed technique based on photographic processing of mechanical tests. This technique is applicable for monitoring surface displacements and strains in masonry walls. The fundamental concept of the DIC method is a non-contact optical strain measurement technique. In this approach, digital photographs of the masonry wall at various loading stages are compared using computer software. These images are utilized to track the full-field deformation of the surface [13]. DIC has been employed in various engineering fields to measure displacement and strain in large specimens within laboratory projects, demonstrating its simplicity for post-processing [13]. This study subsequently evaluated whether DIC is equally accurate for smaller specimens and whether it can provide similarly detailed results.

3.2.1 Image analyse DIC results

The images captured during the test were processed and analysed using VIC-2D software, which can provide full-field, two-dimensional displacement and strain data through a correlation technique [14]. The deformation capacity, visible damage at various displacement levels and vertical deformation responses of the wall specimen were assessed using the DIC method.

The preparation of images for analysis involved several steps, including importing speckle images into the VIC-2D software, defining the area of interest (AOI), calibrating the scale of the reference image, and determining the subset and step sizes.

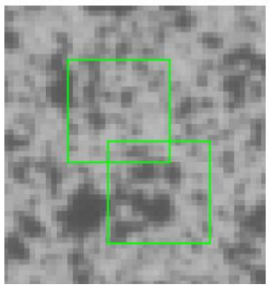

Figure 32 : square facets [15]

An initial reference image of the undeformed specimen was captured. The software then analyses the stochastic pattern and applies square facets on the image. The pixel size for each facet is carefully chosen to balance measurement accuracy with computational efficiency. The AOI was delineated by drawing a polygon on the reference image. The AOI of the tested wall is illustrated in Figure 32. The scale of the reference image was calibrated by defining the exact distance between two known points. By utilizing the relative motion of points within each square facet, the software monitors deformation throughout various stages. The number of stages is limited by the frames per second (FPS) the images were taken with. The

results are visualized for the strain fields to analyse the strain distribution across the specimen and the displacement fields to see how the specimen has deformed. The results are also exported for further analysis to compare with displacements obtained from the potentiometers. Accurate measurement of in-plane displacement within the selected AOI is critical, and the precision of DIC measurements can be influenced by various factors such as the specimen, loading conditions, imaging setup, and correlation algorithm. The facets size directly impacts the correlation algorithm and plays a crucial role in the accuracy of displacement measurements in ZEISS Inspect Correlate [10]. Proper adjustment of the facets size can reduce measurement errors in the DIC method, as the facets size controls the area of the image used to track displacement between images [20]. A smaller facet size results in a finer grid over the AOI.

To validate the DIC results concerning the selected facet and step sizes, the in-plane deformation capacity of the wall at different imposed displacements obtained from DIC analysis was compared against the displacement values recorded by POT_0 and POT_1. The maximum difference between the values obtained from DIC analysis and those from these potentiometers is expressed as the error, calculated using Eq. 8 as described by M. Ghorbani [16]. ΔDIC and ΔLVDT represent the wall deformations obtained from DIC analysis and the measurement instruments, respectively.

$$Error = \left|\frac{\Delta_{DIC}-\Delta_{LVDT}}{\Delta_{LVDT}}\right| \times 100\% \qquad [8]$$

Four of the triplet tests were performed with the aim of applying the DIC method. The second triplet gave the clearest results of them all. For this reason, this one will be used to describe the test/results.

3.2.2 Major strain

Strain is a measure of deformation relative to a predetermined reference stage. Major strain is defined as occurring in the direction with the greatest deformation. The images below show the crack gradually forming between the middle brick and the right brick. This crack propagates from the bottom to the top as the strain increases, ultimately leading to the rapid failure of the specimen due to the brittleness of the materials. This results in a clean break on the surface of the mortar and the brick, exhibiting a type A3 crack pattern as mentioned in paragraph 'Determination of Bond Strength' as seen on Figure 25.

As soon as the crack forms (frame 263), the specimen shifts within the test setup, causing deformation that is too significant for the program to detect on this scale. The structural integrity is lost at a critical load of 0,234 N/mm². After the critical load was achieved, the force was further increased until the friction gave out.

Subsequently, the horizontal load was increased again to continue the testing process to determine the friction coefficient.

Additionally, a crack also forms in the left brick, though it is not noticeable after the test. This demonstrates the subtle movements that occur during the formation of a crack.

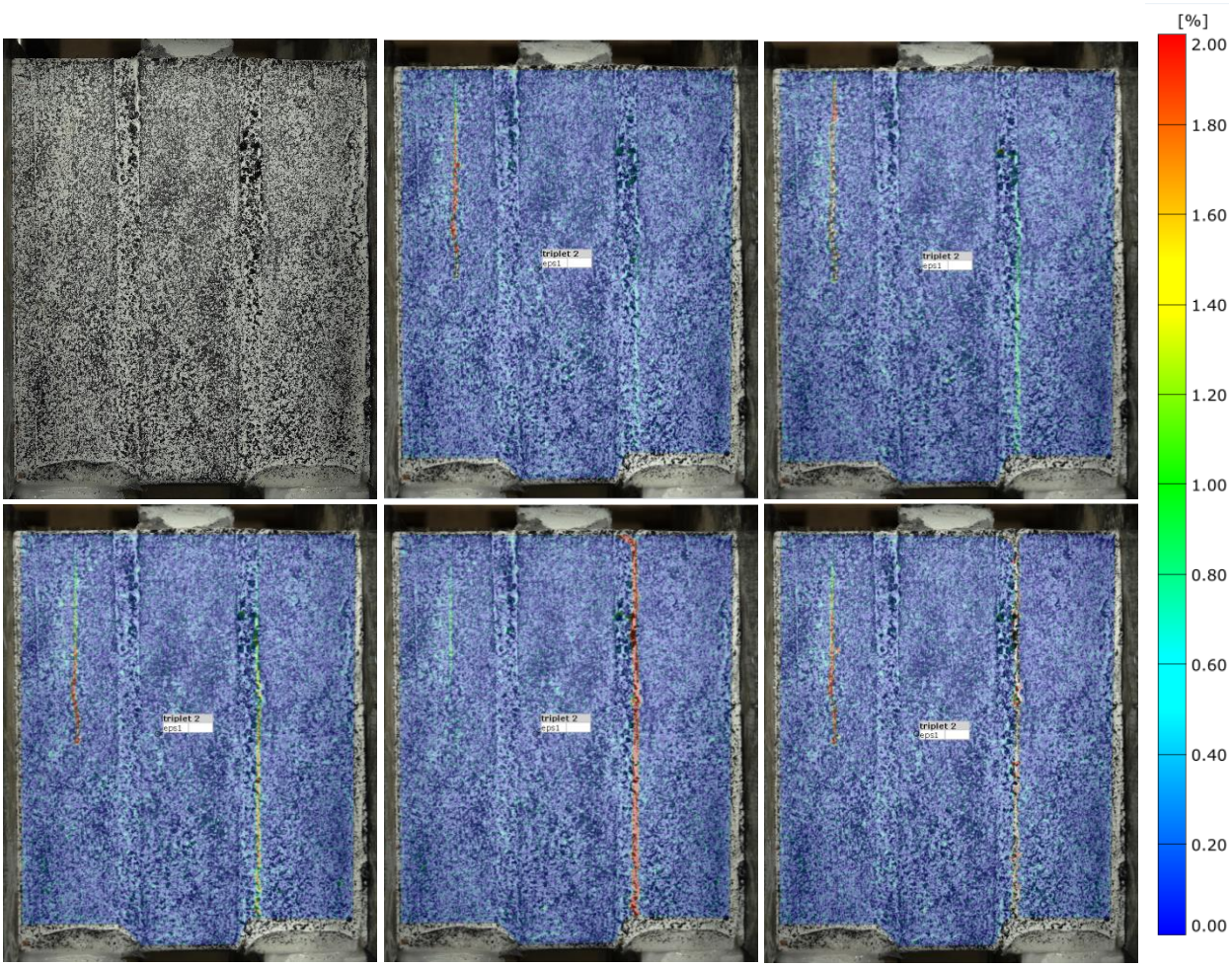

Figure 33 : major strain of triplet 2 obtained by DIC (frames 257 – 259 – 263 – 264 - 276)

3.2.3 Tracking Displacement and Correlating Data from Potentiometers

In this analysis, the relative displacement is determined of specific points on the specimen that correspond to potentiometers mounted on the backside. The data obtained from these potentiometers are linked with the values recorded using ZEISS INSPECT [10] to verify the precision of the program in determining exact time and displacement during all stages of the experiment. This allows for the drafting of a graph representing shear stress as a function of time.

As illustrated in Figure 38, the entire setup shifts slightly in an anticlockwise direction right up until the crack formation. After the crack occurs, the setup nearly stabilizes back to its original position before beginning to turn in a clockwise direction. This phenomenon is also evident in Figure 36 and Figure 37, where the crack is fully formed at frame 263.

There are a couple potential sources of error that have an impact on the accuracy of the results. The FPS of the camera was not constant during the whole test, also the exact moment in time of the picture was not registered although the sensors from the lab register to the millisecond. If this data was available, it would improve the accuracy enormously.

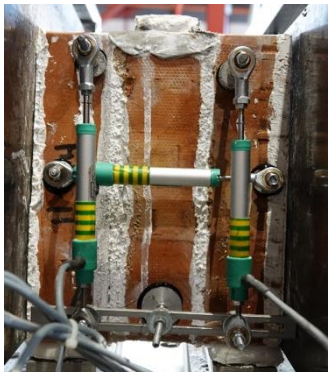

Figure 34 : triplet 2 in test set-up and after failure

Figure 35 : fully formed crack after testing the shear strength

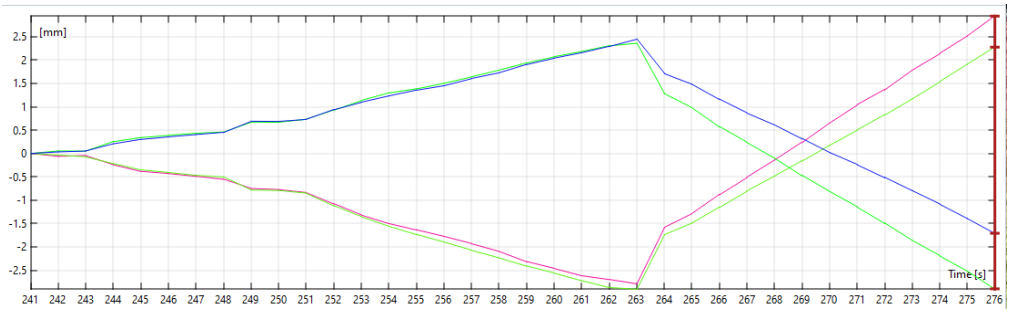

Figure 36 : triplet 2 _ X-displacement

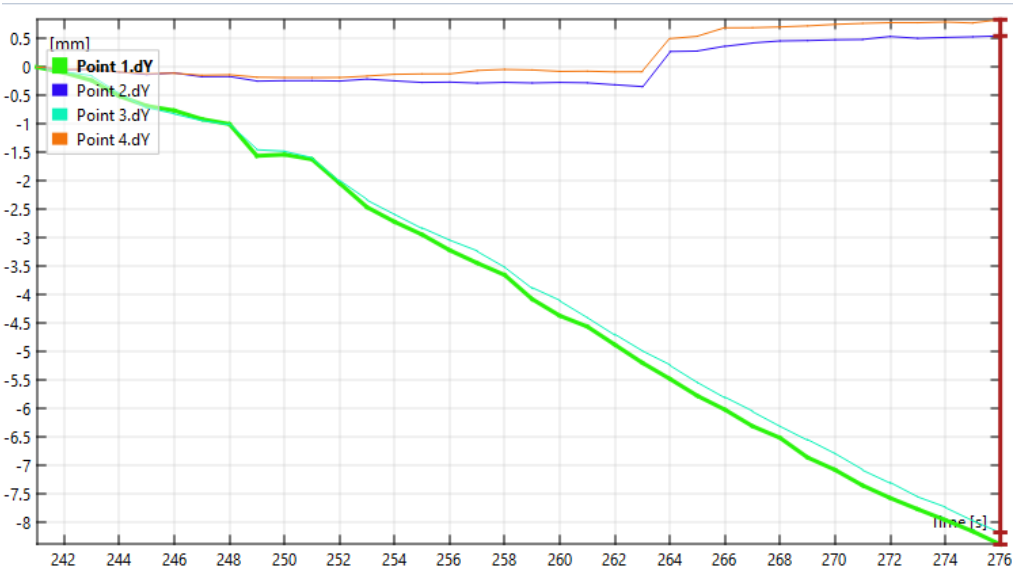

Figure 37 : triplet 2 _ Y-displacement.

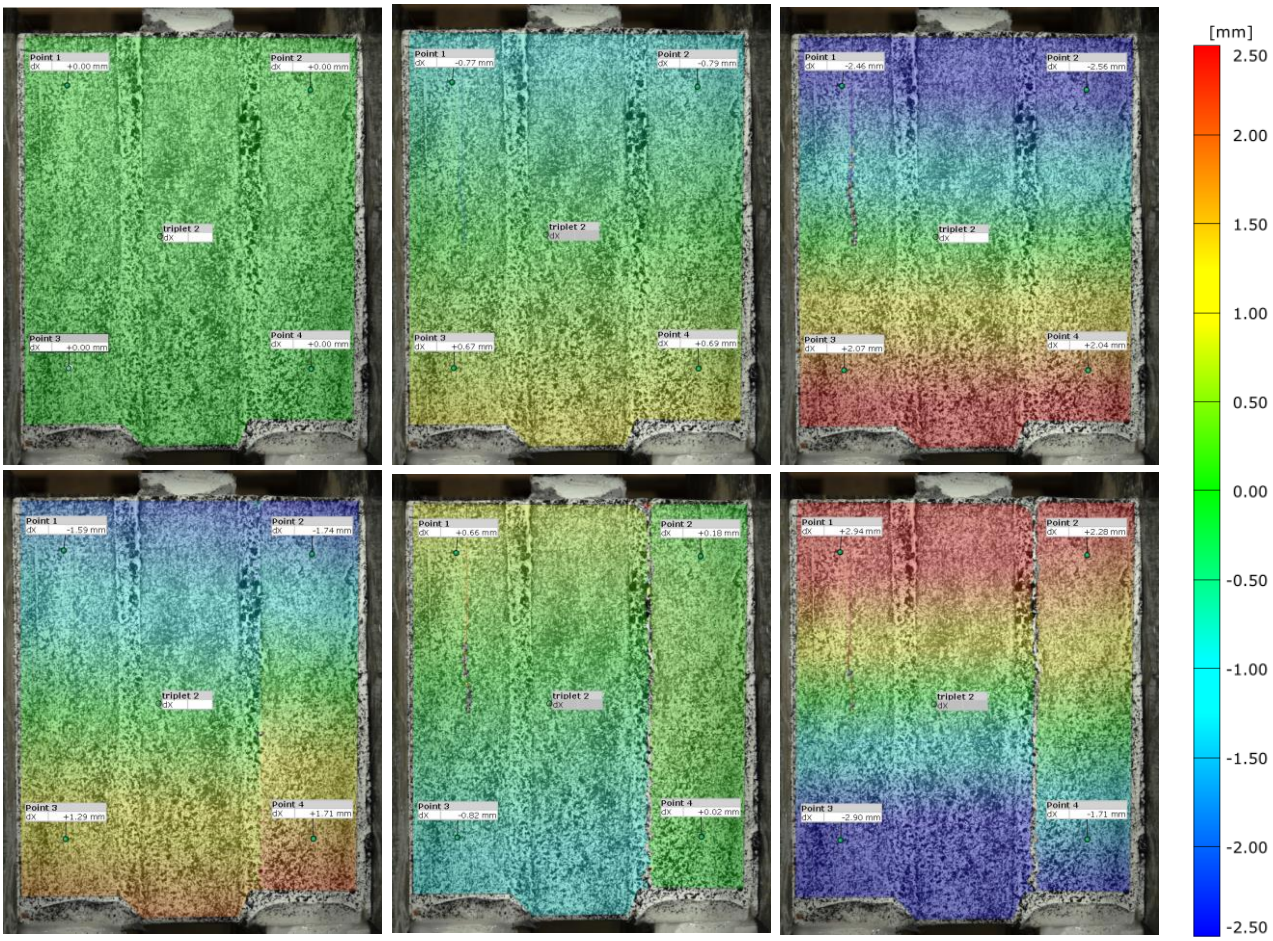

Figure 38 : triplet 2 _Displacement (Frames 240–250–260–263(crack)–270–275)

3.3 Shear strength test (Translational) data

Potentiometers measure displacements, while the shear strength was assessed by plotting the loads recorded by a load cell integrated into the actuator against the displacements measured by the potentiometers. The peak force, corresponding to the shear strength, was then identified. Measurements, initially obtained in volts, were converted to kN. Displacement values, applied forces, shear tress and normal force were recorded as functions of time. The peak shear stress was identified, which corresponds to the point where the triplets exhibit cracking and loses their resistance. The associated time, normal stress, vertical force and displacements were also determined. The relation between these variables is illustrated in the graphs presented, from figure 39 to figure 43. Peak shear stress values are highlighted in orange, along with their corresponding relational value. The data demonstrates that the shear stress graph aligns with the graph of the increasing force, and the normal stress and horizontal force graphs are consistent with expected outcomes.

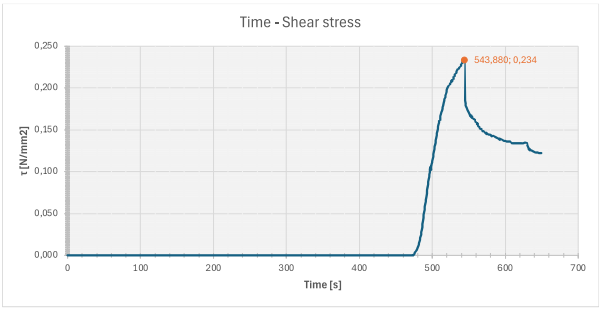

Figure 39 :Time - shear stress relation - Triplet 2

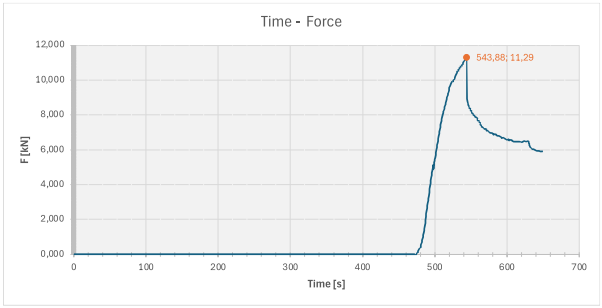

Figure 40 : Time - force relation – Triplet 2

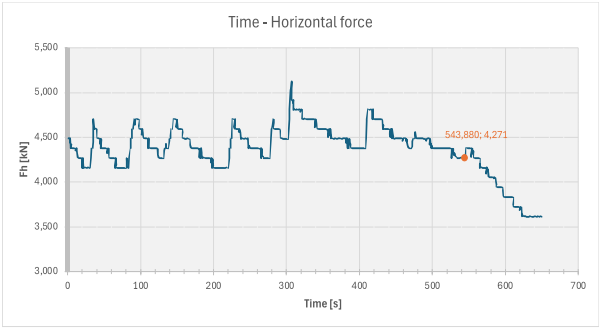

Figure 42 : Time - horizontal force relation – Triplet 2

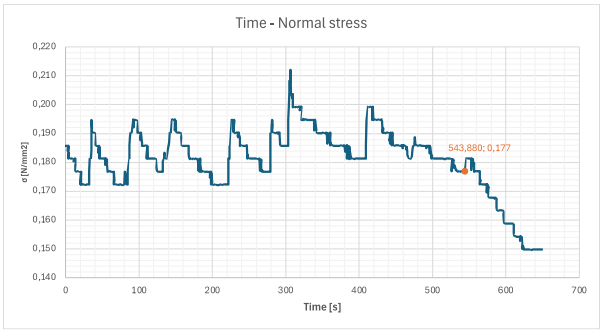

Figure 41 : Time - normal stress relation - Triplet 2

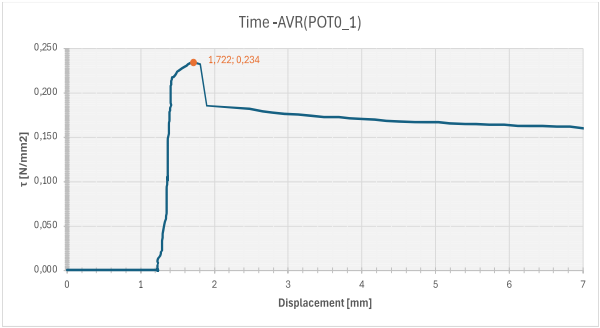

Figure 43 : Time - average displacement between POT_0 and POT_1 - Triplet 2

Table 7 : Values associated with the peak shear strength value

Shear peak with associated values			
Definition	*Symbol*	*Value*	*UM*
Peak shear strength	τ_{peak}	0.2337	N/mm^2
Time	T	543.88	s
Normal stress	σ	0.1768	N/mm^2
Vertical force	F	11.290	kN
Horizontal force	F_h	4.2709	kN
Peak displacement POT_0	d_0	0.3415	mm
Peak displacement POT_1	d_1	3.1020	mm
Average from POT_0 and POT_1	AVR(POT0_1)	1.7217	mm

3.4 Synchronisation measurements with DIC-program

To verify the accuracy of the photos in the DIC program, a comparison was made with the actual experimental values measured by the potentiometers. The goal is to determine whether the DIC system is as accurate as the potentiometers, potentially allowing the latter to be omitted in future tests. Replacing potentiometers with photos would be advantageous if accurate results can be obtained.

A snapshot of the frame, frame 263, where the crack initiates was taken in the DIC system. Several photos were selected within a specific time interval around this frame. The same time interval was then analysed in the experimental data.

For the second triplet test, 36 photos (frames 241 to 276) were selected and analysed. The values obtained from the DIC program indicate a specific time interval with corresponding frame numbers and displacements of the designated points within the DIC system, which are about three in total. The following formula, Eq. 9, was used to derive a factor, R_DIC, based on the DIC values for comparison with the experimental data.

$$R_{DIC} = c - \frac{(A+B)}{2} \qquad [9]$$

where

A = the upper point of the potentiometer on the left, in the DIC;
B = the upper point of the potentiometer on the right, in the DIC;
C = reference point, positioned in the middle on the bottom of the triplet, in the DIC.

The data obtained from the experimental analysis were also converted into a factor, R_DATA, for comparison with the DIC factor. This factor represents the average value obtained from the two potentiometers under focus, calculated following Eq. 10.

$$R\_DATA = \frac{POT\_0 + POT\_1}{2} \qquad [10]$$

These values were then linked and plotted in an overlapping graph. The orange markers represent the values from each frame in the DIC system, while the blue graph shows the values obtained from the experimental phase. These values were plotted in a shear-stress graph and after converted into a time-relative displacement graph, illustrated in Figure 44 and Figure 45 correspondingly.

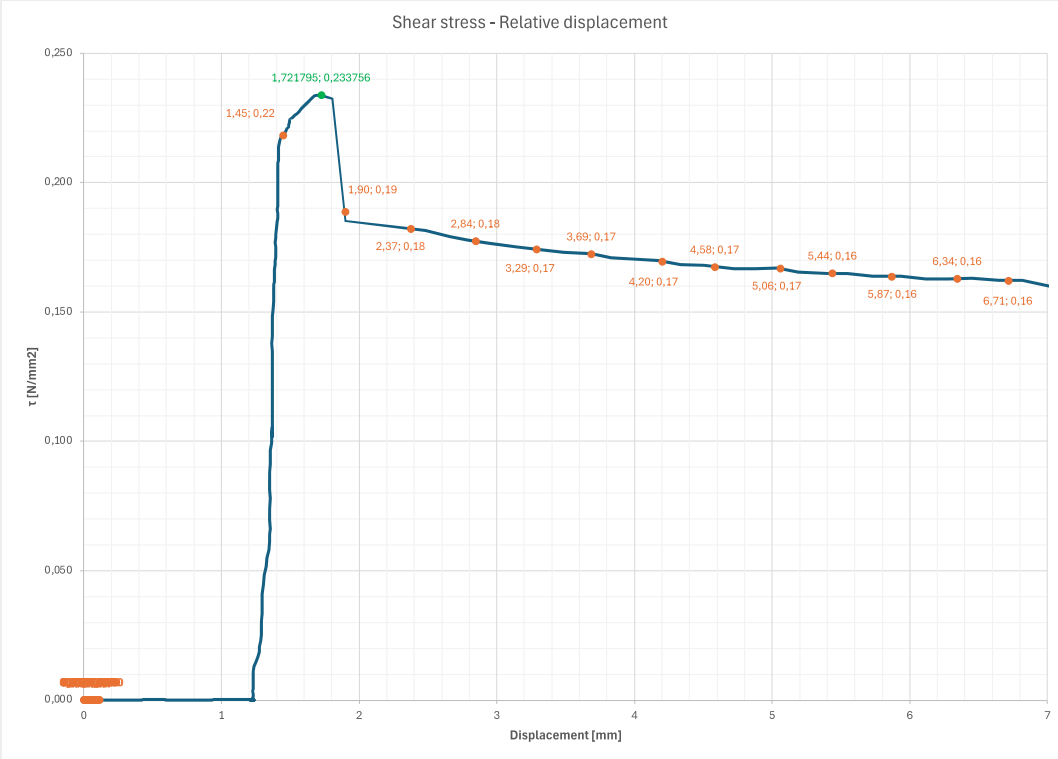

Figure 44 : R_DIC and R_DATA combined values for shear stress - relative displacement relation

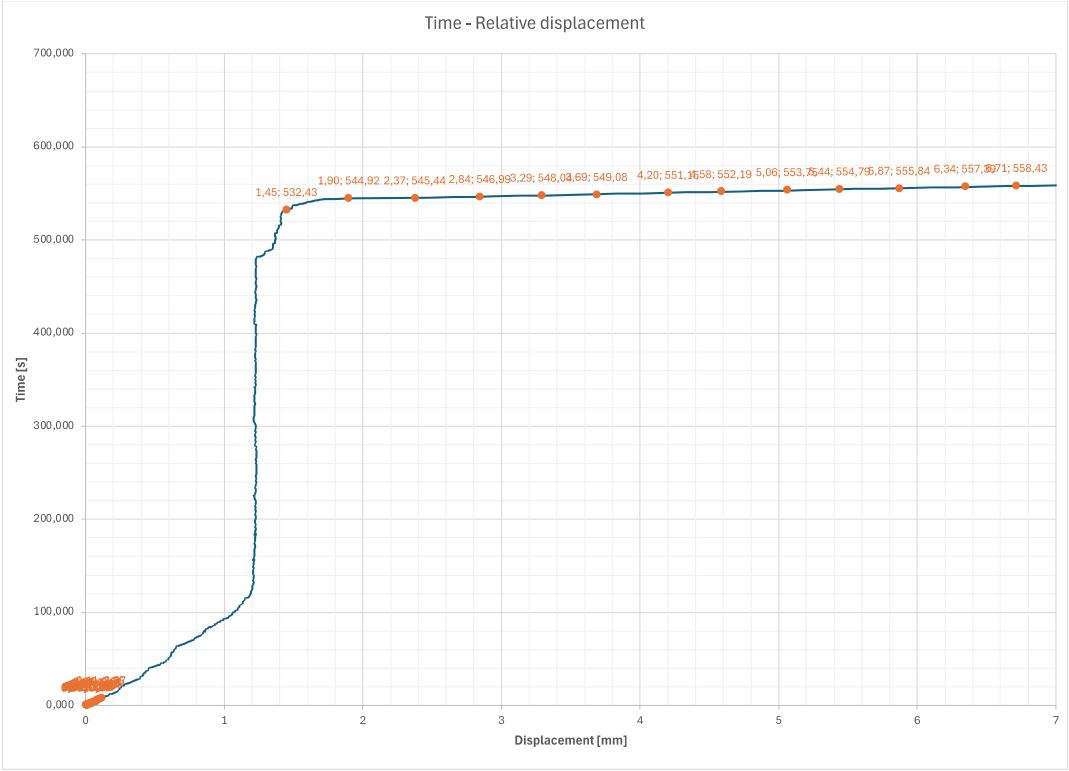

Figure 45 : R_DIC and R_DATA combined values for time – Relative displacement relation

4 Test setup gable

The following paragraph provides a description of the test setup used for this research. Detailing the individual components and their placements. The test setup is designed to ensure precise control over all boundary conditions, minimize uncertainties, and facilitate a comprehensive analysis of the out-of-plane behaviour. The shake table tests are conducted at the EUcentre laboratory using the 9D shake table. This setup allows for independent movement of the top and bottom of the gable, simulating the interaction between the gable and the roof they support.

Three full-scale gable walls were dynamically tested in the out-of-plane (OOP) direction during this phase of the campaign. Each specimen was tested differently using the shaking tables. The aim of these tests was to subject the first gable wall to an acceleration with a specific amplitude, where the top and bottom planes of the shaking table move together, maintaining the same phase and amplitude. This first test is assumed to be stiff. The subsequent tests are considered semi-stiff and flexible for the second and third tests, respectively.

4.1 Boundary condition and seismic inputs

The primary objective of these tests was to accurately simulate and control the boundary conditions of a single masonry gable, thus isolating its seismic response behaviour. The 9D shaking table was crucial in this setup, enabling the application of seismic inputs both at the base and the top of the gable walls. This setup allowed for a precise simulation of the diaphragm conditions of the roof, whether stiff, semi-stiff or flexible.

The simulation is intended to replicate the conditions of a terraced house located in the Groningen region of the North-East Netherlands. The majority of existing buildings in the region are low-rise unreinforced masonry (URM) structures, which were not originally designed to withstand seismic loads. Earthquakes in this region are typically shallow and induced by gas extraction, characterized by lower amplitude ground motions. After simulating the Groningen scenario, the experiment will proceed with higher seismic intensities to simulate conditions associated with more severe earthquakes.

The tests aimed to expose the first gable wall to an acceleration with a specific amplitude, where both the top and bottom planes of the shaking table moved together, maintaining the same phase and amplitude. For the second gable, the motion at the top table was simply amplified relative to the base and the motions remained in phase with each other. In contrast, for the third gable, the motion at the top table was both out of phase and amplified relative to the bottom table.

4.1.1 Basic modelling assumptions

The input acceleration of the top and bottom shaking table was generated from the research completed by TUDelft and the University of Pavia. These contains the input signals for out-of-plane seismic testing of the three gable walls for stiff, semi-stiff and flexible. These assumptions were made based on a basic terraced house from the Groningen area in The Netherlands. For the configuration with flexible roof structure were linear elastic orthotropic shell elements employed to simulate the behaviour of the plywood timber roof. For the stiff setup, linear elastic isotropic shell elements were simulated to conduct a concrete slab. The last configuration, the semi-stiff one, was simulated with macro-elements which represents the dissipative response of a timber roof retrofitted with plywood panels, calibrated against the experimental tests on the strengthened roof pitch in [17].

Configuration with flexible roof structure: $E_x = E_y = E_z = 10\ 000$ MPa,
$G_{xy} = G_{yz} = 625$ MPa

Configuration with stiff roof structure: $E = 30\ 000$ MPa
$G = 13\ 000$ MPa

Configuration semi-flexible:

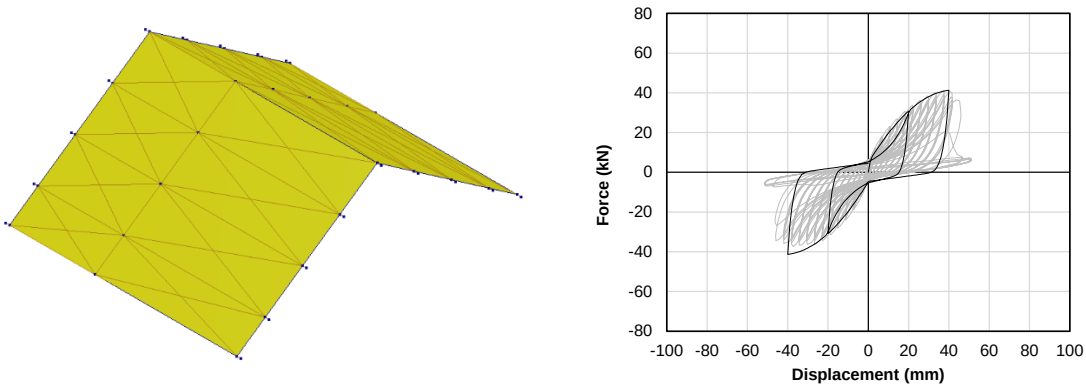

Figure 46: Macro-elements simulation of a plywood timber roof

4.1.2 Peak ground acceleration (PGA)

The input accelerations, representing the induced seismicity, are provided in meters per second squared (m/s²). The time increment for data recording is set at 0.01 seconds, with the recording commencing at 0 seconds rather than at 0.01 seconds. In all three scenarios, the recording for the bottom shaking table remains consistent. However, for the stiff roof scenario, the records for both the top and bottom tables are identical. Additionally, the table motions for the stiff roof scenario were generated based on tectonic seismicity [17].

Configuration with flexible roof structure: PGA = 0.30g (near-collapse)

Configuration with stiff roof structure: PGA = 0.30g (damage limit state)

Configuration semi-flexible: PGA = 0.30g (damage limit state)

4.1.3 Accelerograms of attic floor and gable top

For the flexible and semi-stiff roof structures, the accelerograms for the top gable have been adjusted with an amplification factor to account for the height difference between the ridge beam at the top of the gable (2900 mm) and the upper platform (3750 mm). Specifically, the top gable accelerograms are computed using the formula:

$$a_{top} = \left(\frac{a_{ridge} - a_{base}}{2900}\right) \times 3750 + a_{base} \quad [\text{m/s}^2] \qquad [11]$$

Where a_{base} = represents the accelerograms at the base [m/s²];
a_{stiff} = represents the accelerograms at the ridge beam [m/s²].

The configurations below, representing the acceleration inputs for each gable. In case of the stiff roof structure, the target was to apply the same motion on the top and bottom tables. So theoretically, both right and left images should be the same outcome, shown in Figure 48. Furthermore, the relative displacement time-histories of the stiff roof diaphragms, shown in Figure 51, indicate almost no relative motion between them. Since the top and bottom motions are identical, no relative displacement is expected.

Configuration with flexible roof structure:

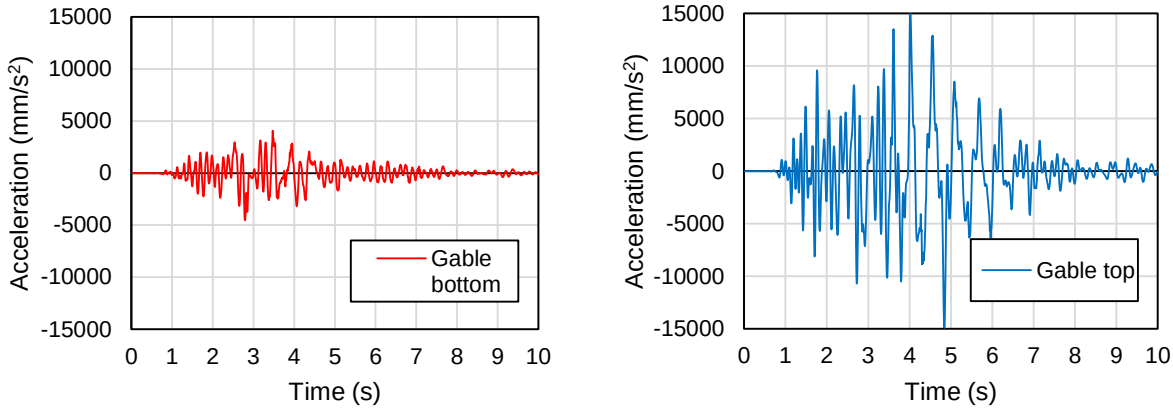

Figure 47 : Accelerogram flexible gable bottom & top

Configuration with stiff roof structure:

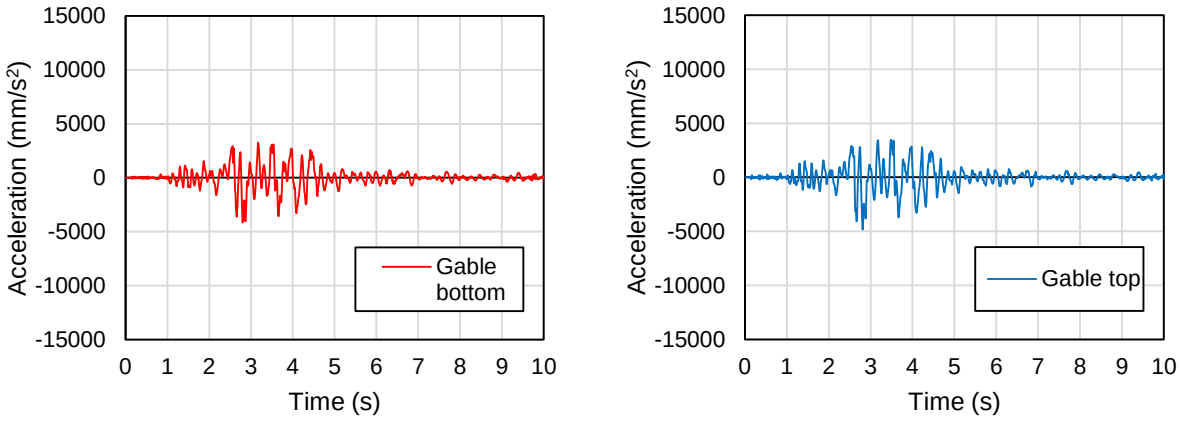

Figure 48 : Accelerogram stiff gable bottom & top

Configuration semi-flexible:

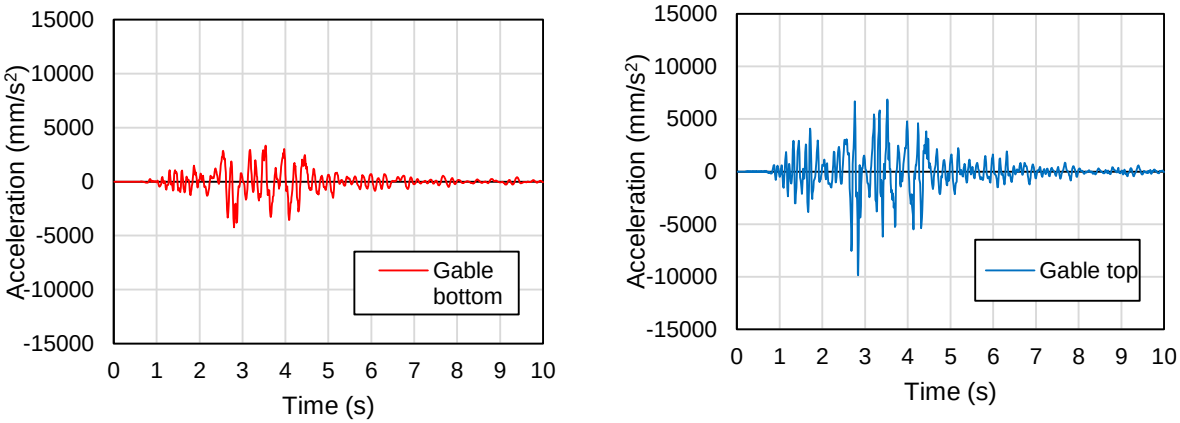

Figure 49 : Accelerogram stiff gable bottom & flexible top

4.1.4 Relative displacement time-histories of the roof diaphragms

Configuration with flexible roof structure:

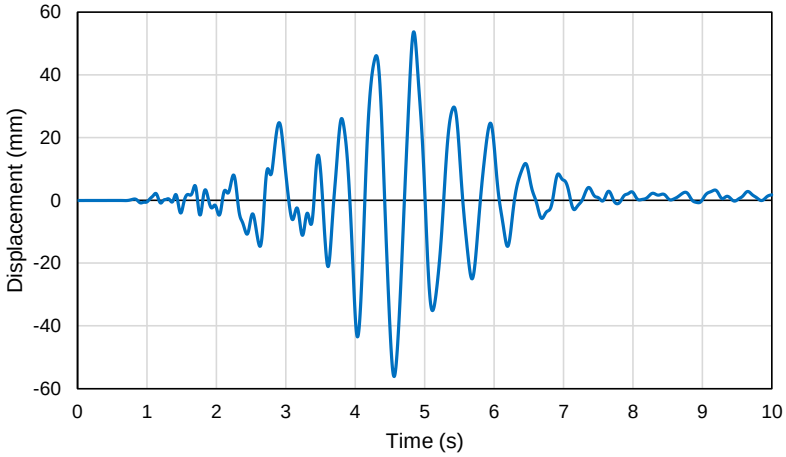

Figure 50 : Relative displacement time-histories of flexible roof structure

Configuration with stiff roof structure:

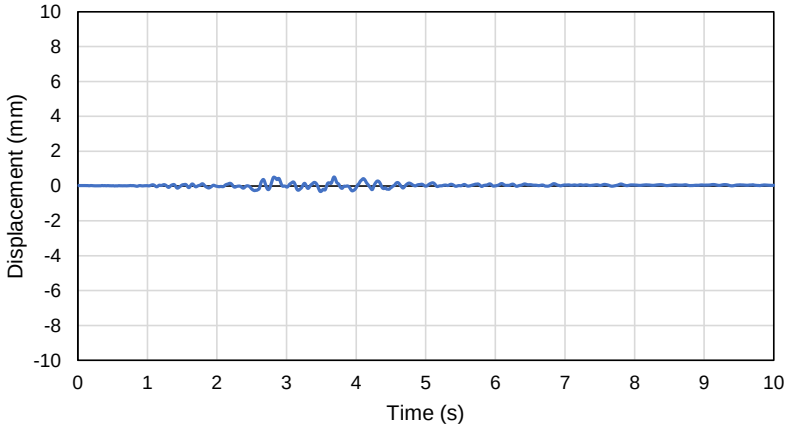

Figure 51 : Relative displacement time-histories of rigid roof structure

Configuration with semi-stiff roof structure:

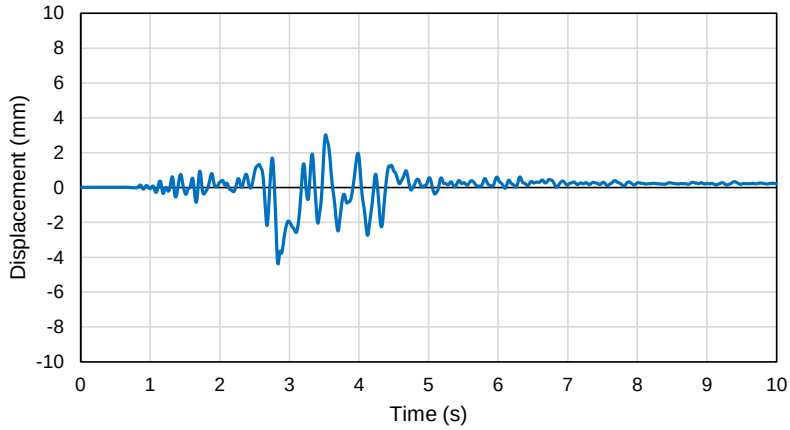

Figure 52 : Relative displacement time-histories of semi-rigid roof structure

4.1.5 Response spectra of the input signals (2% damping)

For the flexible and semi-stiff roof structure top gable accelerograms, the spectra derived from the signals already incorporate an amplification factor similar to that in Eq. 11. This factor accounts for the height difference between the ridge beam at the top of the gable (2900 mm) and the upper platform (3750 mm) [17].

Configuration with flexible roof structure:

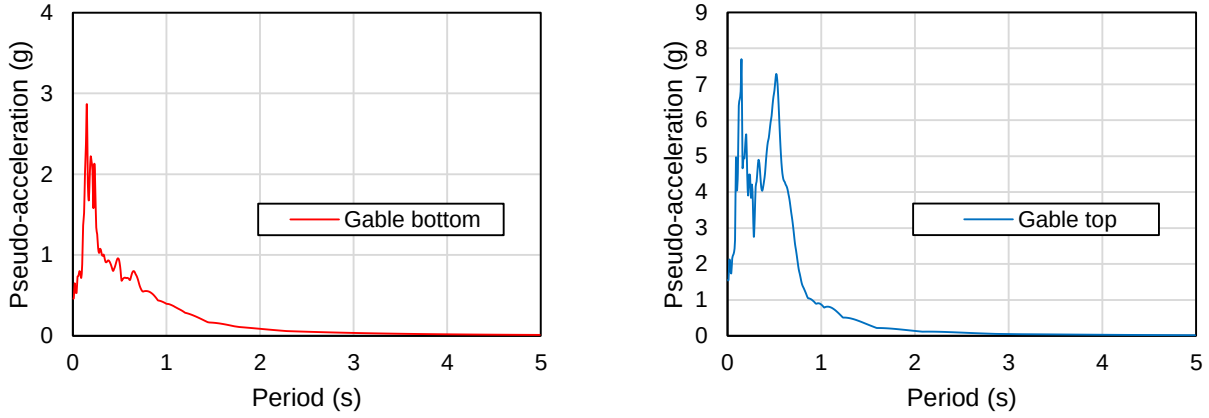

Figure 53 : Response spectra input data flexible roof

Configuration with stiff roof structure:

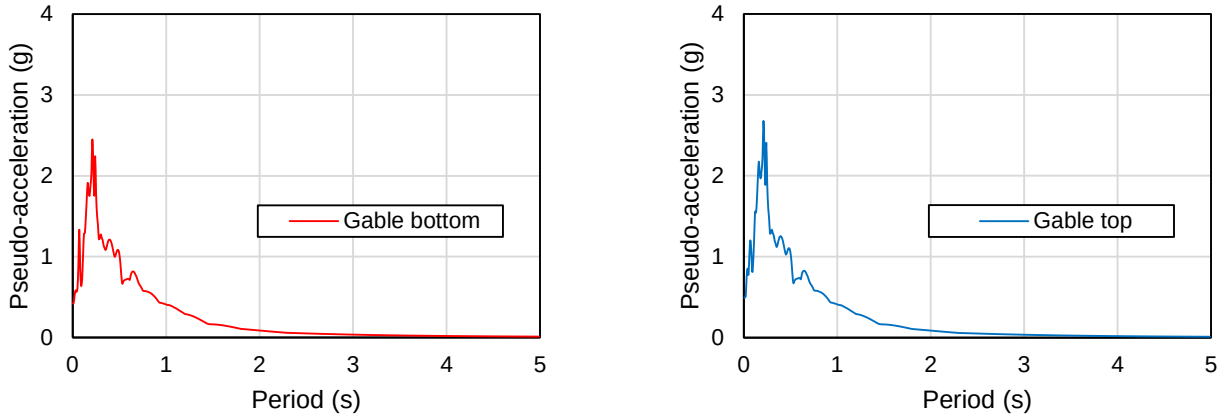

Figure 54 : Response spectra input data rigid roof

Configuration with semi-stiff roof structure:

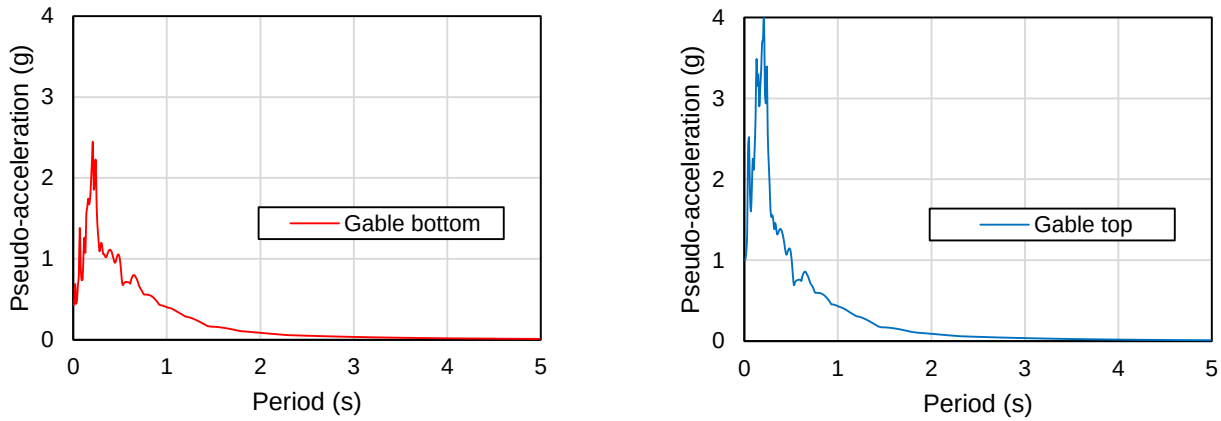

Figure 55 : Response spectra input data semi-stiff roof

4.2 Overview components

To determine the setup, FUSION360-software was used, which allowed for the quick and precise dimensioning of all elements, including the vibrating table. Figure 56 provides an overall view of the elements used.

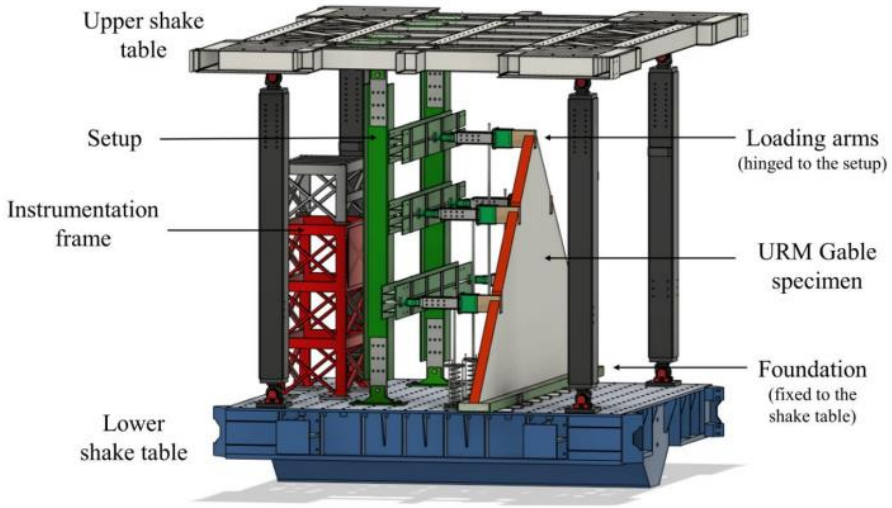

Figure 56 : key components shake table (fusion 360)

The constructed gables consist of a single-leaf solid brick masonry, shaped as an isosceles triangle with a base spanning of 6 meters and a height of 3 meters. It is securely anchored to the reinforced concrete foundation of the shaking table using steel bolts. Additionally, a mortar bed-joint is implemented between the bottom layer of the gable and the foundation for enhanced structural stability.

The interaction between the structure and the roof will be simulated by manipulating the motion of both the bottom and top platforms of the 9DLAB shake table. Truss beams, hinged at the top and bottom to these platforms, will be supported at the opposite end by the masonry gables. Horizontal displacements will be determined by interpolating the displacements induced by the two platforms during the test.

Timber elements will be embedded within the masonry, exerting a vertical pre-load to mimic real roof conditions. To maintain a consistent load, the loading points will be spring-loaded. No metal anchors or other connectors will be utilized in this simulation.

All bolted joints were designed in accordance with the procedures specified in Eurocode 3 for frictional joints [18], specifically utilizing preloaded, high-strength bolts ranging from grade 8.8 to 10.9. To enhance efficiency during assembly, bolt dimensions were selected to minimize variability in diameters, thereby saving time

and reducing the likelihood of errors. The design of multiple steel connections and joints, including the placement of holes and the spacing between them, was guided by the recommendations provided in Eurocode 3 [18].

4.2.1 Uprights

The vertical steel beams were designed to provide sufficient stiffness to the setup frame, ensuring that the rest of the structure remains at the correct height during the movement of the shaking table.

4.2.1.1 Design

First, the deflection of the elements was calculated leading to the selection of an HEB300 profile. The forces were determined by considering one-fifth of the gable's mass, as there are five loading arms excluding the lower part of the gable, which is fixed to the foundation of the beam. These forces were then multiplied by an acceleration of 2g and a safety coefficient, increasing the value by 20%. The profile taken for the project showed a max inflection lower than 0.5 mm.

$$F = \frac{mass_{gable}}{5} \times 2g \times 1.2 = 9\ kN \qquad [12]$$

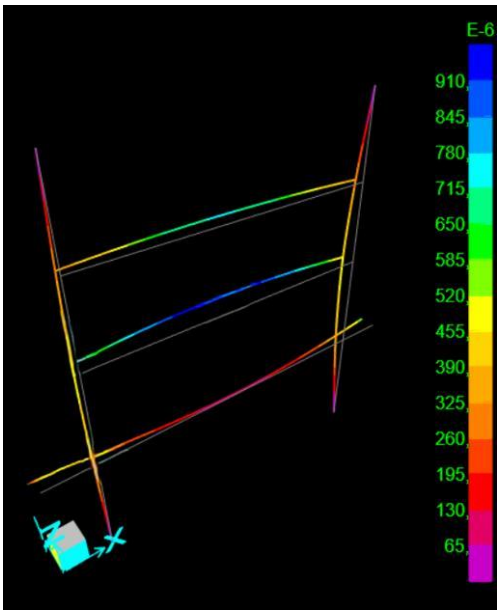

Figure 57 : Inflection of the frame dimensioned in SAP2000

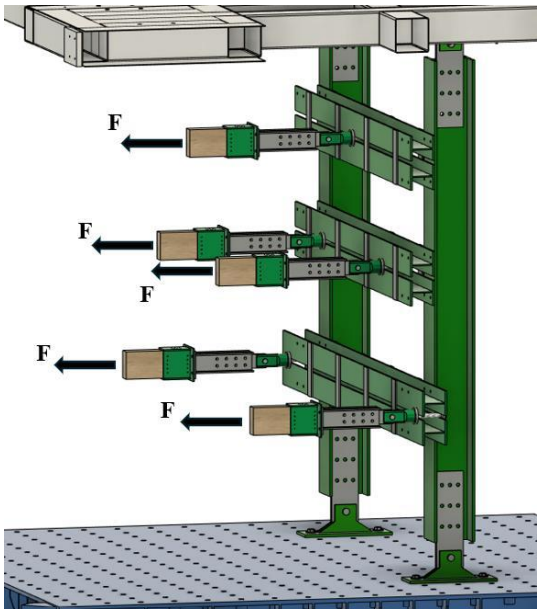

Figure 58 : Forces applied to the model, showed in Fusion360

4.2.1.2 Joints

At the top and bottom of the beams, two 10 mm thick steel plates were welded together to enclose the web, forming hinges at both ends of the uprights as shown in Figure 59. The connection was secured with 18 M24 grade 8.8 bolts, with 9 bolts on each side. The characterizations of these bolts are previewed in appendix A.

The preloading force ($F_{p,Cd}$) and slip resistance (F_{Rd}) were calculated with the formula following Eq.13 and 14., used in the context of Eurocode 3 (En 1993-1-8) [18] for the design of steel structures and bolted connections, where it helps in determining the slip resistance of a joint under applied loads.

$$F_{p,Cd} = \frac{0.7 \times f_{tb} \times A_s}{\gamma_{M7}} \text{ [kN]} \quad [13] \qquad F_{Rd} = \frac{k_s \times N_{pdt} \times \mu}{\gamma_{M3}} \text{ [kN]} \quad [14]$$

Where A_s = the tensile stress area of the bolt [mm²];
f_{tb} = the ultimate tensile strength of the bolt material [MPa];
γ_{M7} = the partial safety factor for the bolt material.

and k_s = a slip factor that accounts for the type of frictional contact surface preparation;
μ = the coefficient of friction between the contact surfaces;
N_{pdt} = the number of effective friction surfaces in the joint;
γ_{M3} = the partial safety factor for materials.

4.2.1.3 Adaptability

To allow for some movement of the elements, slotted holes have been provided, applying the principle of a mortise and tenon joint. This also facilitates the assembly process. The hinges at the top are secured to the shaking table using plates fastened with eight M20 screw rods, allowing the position to be adjusted to create space for the overhead crane used during the assembly process. The hinges are carefully aligned with the hinges of the shake table's connecting rods, which is essential to ensure the proper load distribution.

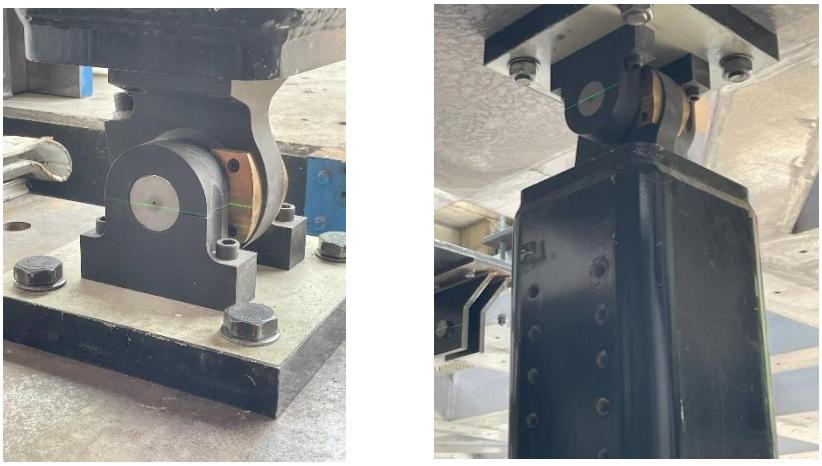

Figure 59 : Mortise and tenon joint

4.2.1.4 Horizontal steel beams

The horizontal elements consist of two HEB180 profiles assembled with welded plates. The purpose of these elements is to provide support to the steel arms that simulate the roof purlins. The lower beam is longer than the other due to the distance between the hinges.

4.2.1.5 Design

As described within the previous section, calculations were performed on the horizontal elements to determine the maximum deformations. The ends of the longest beam were scaled by welding a steel plate to increase the stiffness of the profile.


Figure 60 : Horizontal steel beams

4.2.2 Loading arms

The steel arm consists of three components: a hinge that attaches it to the setup, two UPN140 profiles secured to a plate with an opening for the hinge pin and a bow profile that functions as a support for the purlins. Considering the loads applied by the springs, which will be detailed in the following paragraph, as well as the horizontal force resulting from the dynamic effects on the gable wall, the moment on the arm at the box profile housing the purlin was calculated. Consequently, the shear force on the screws securing it was also determined.



Figure 61 : the components of the loading arms

4.2.3 Springs

To apply a vertical load to the gable walls springs attached to mechanical arms were used. This setup simulated the realistic load that a roof would exert on the gable. As the gable pivoted on its base during the test, the support conditions of the beams altered, resulting in the load being concentrated at a single point rather than being evenly distributed across the entire thickness. Despite this shift, the applied load remained perpendicular to the shaking table, reflecting the accurate simulation of real-world conditions.

The springs required testing to determine their stiffness. Springs 1, 2, 4, and 5 were selected for use with the outer purlins, while spring 3, with higher stiffness, was allocated to the top purlin. The selection of these springs was based on their availability in the lab, resulting in spring 3 being different from the others. To maintain symmetry, spring 3 was positioned at the centre of the structure.

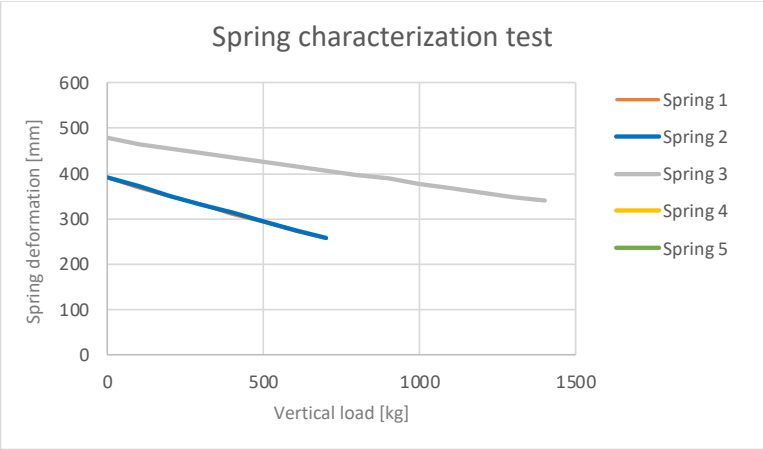

Figure 62 : Deformation of the springs under determined loads

The final length of the spring was measured to ensure proper compression of the spring. The goal of this process was to ensure sufficient friction force between the wood and masonry to promote out-of-plane failure while preventing the entire gable from rocking. The minimum required friction force was calculated in advance using virtual work approach, selecting the mechanism with the lowest energy demand from various options.

Table 8 : spring properties

Spring	*Stiffness*	F_{gable}	F_{spring}	Δ_{eff}	Δ_{limit}	*Gap*	L_{fin}
[#]	*[N/mm]*	*[kN]*	*[kN]*	*[mm]*	*[mm]*	*[mm]*	*[mm]*
1	48.15	4.20	8.40	174	221	47	217
2	50.61			166	221	55	225
3	88.86			95	248	153	383
4	47.30			178	225	47	217
5	50.35			167	222	55	225

5 Placement of sensors

The determination of the number and positioning of the measurement instruments was based not only on the key areas of interest for monitoring, but also on the importance of protecting the instruments from damage during and after the collapse of the specimen. This consideration is crucial, given that multiple tests are conducted serially with short intervals in between. The instruments were placed both on the setup and directly on the specimen to accurately monitor the displacements and behaviour of the specimen.

Figure 63 provides an overview of the instruments used with their respective locations for monitoring the gable wall. The setup includes accelerometers, wire potentiometers, standard potentiometers and optical acquisition systems. These instruments will be furthers explained in the following section.

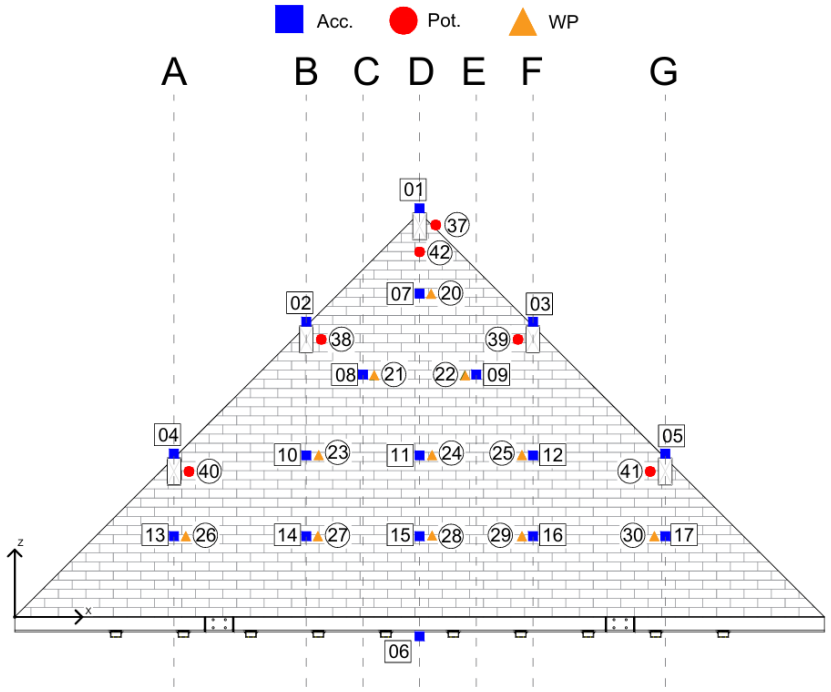

Figure *...men*

5.1 Used instruments

5.1.1 Accelerometer

An accelerometer measures the vibration or acceleration of motion of a structure. A hypothesis was previously formed regarding the failure mechanism of the triangular façade to be tested. Based on this hypothesis, the number and positioning of accelerometers were determined. A schematic overview is shown in Figure 64.

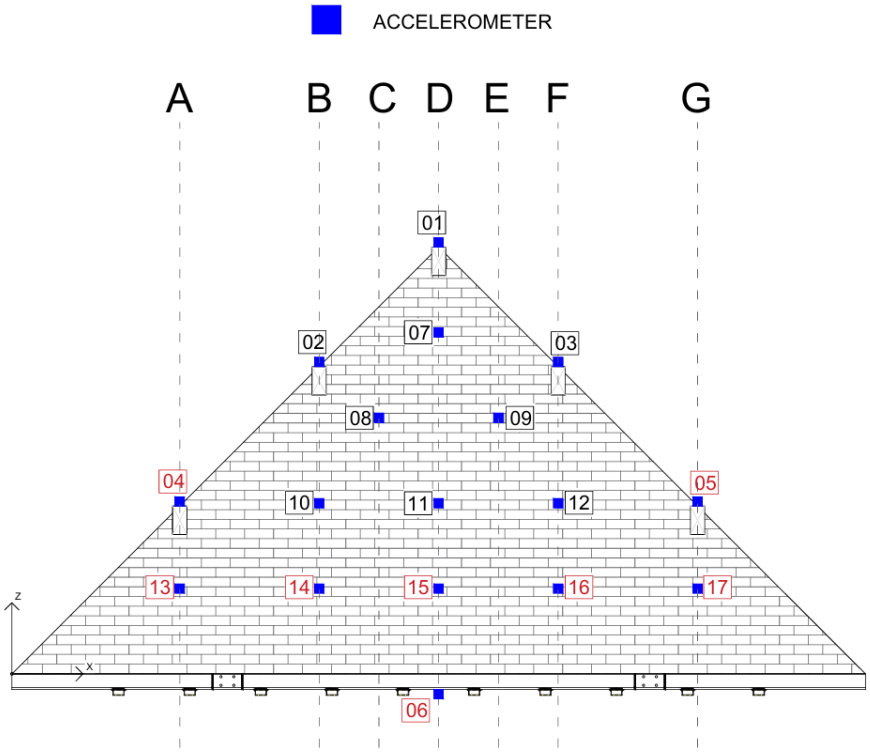

Figure 64 : Schematic overview of the accelerometers placed on the gable wall specimen

Accelerometers with a capacity of 2g were placed at the base of the façade and on the shaking table itself, highlighted in red, due to the expectation of lower amplification in these areas. The remaining accelerometers have a capacity of 6g, which is necessary for the tests to be conducted. The instruments numbered 01 through 05 correspond to those positioned on the purlins, while number 06 refers to the instrument directly placed on the shaking table.

Figure 65 : Accelerometer placed on the purlin

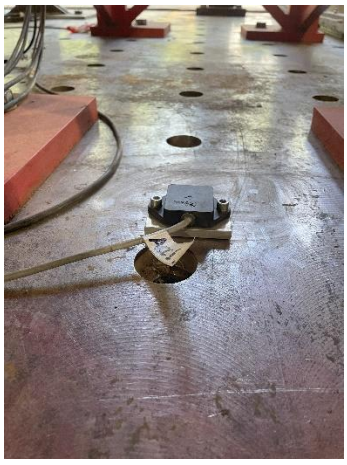

Figure 66 : Accelerometer placed on the shaking table

Influence zones of the specimen were identified based on logical assumptions, this distribution is shown in Figure 67. Corresponding masses were then associated with each instrument, detailed in Table 9.

Table 9 : Accelerometers and determined lumped masses

Name	*Description*				*Position*	
[#]		*Capacity [g]*	*Section*	*Height*	*X [mm]*	*Z [mm]*
00	Time [s]	-	-	-	-	-
01	Ridge beam (X, Y,Z) Acceleration [g]	6	D	-	3000	3000
02	Load-bearing beam (X) Acceleration [g]	6	B	-	2160	2160
03	Load-bearing beam (X) Acceleration [g]	6	F	-	3840	2160
04	Load-bearing beam (X) Acceleration [g]	2	A	-	1180	1180
05	Load-bearing beam (X) Acceleration [g]	2	G	-	4820	1180
06	Shake table	2	D	-	3000	-150
07	Gable wall (X) Acceleration [g]	6	D	4/4	3000	2400
08	Gable wall (X) Acceleration [g]	6	C	3/4	2580	1800
09	Gable wall (X) Acceleration [g]	6	E	3/4	3420	1800
10	Gable wall (X) Acceleration [g]	6	B	2/4	2000	1200
11	Gable wall (X) Acceleration [g]	6	D	2/4	3000	1200
12	Gable wall (X) Acceleration [g]	6	F	2/4	4000	1200
13	Gable wall (X) Acceleration [g]	2	A	1/4	1250	550
14	Gable wall (X) Acceleration [g]	2	B	1/4	2200	550
15	Gable wall (X) Acceleration [g]	2	D	1/4	3000	550
16	Gable wall (X) Acceleration [g]	2	F	1/4	3800	550
17	Gable wall (X) Acceleration [g]	2	G	1/4	4750	550
18	Setup behind top hinge [g]	6	-	-	-	-
19	Instrumentation frame [g]	2	-	-	-	-

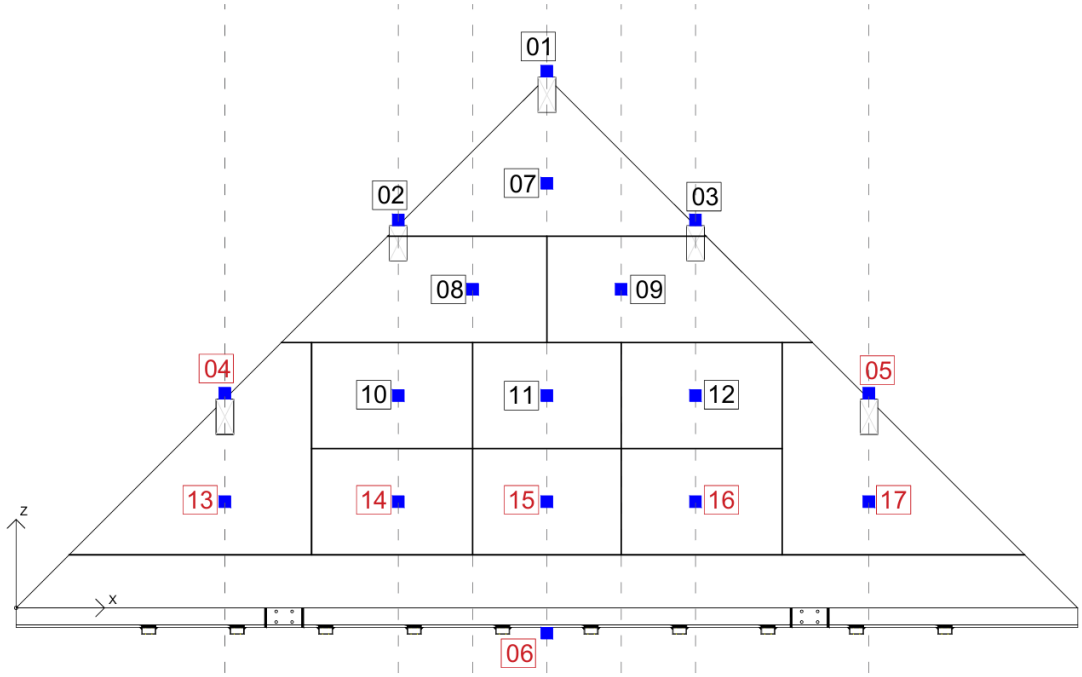

Figure 67 : Lumped mass distribution

Some accelerometers were also installed on the setup's frame to monitor its behaviour. These are positioned behind the hinge of the upper horizontal steel beam, as indicated in Figure 68, and on the instrumentation frame located directly behind the setup as shown in Figure 69.

Figure 68 : Accelerometer applied on the instrumentation frame

Figure 69 : Accelerometer located on the upper steel beam of the setup frame

5.1.2 Wire potentiometer

A potentiometer is a tool used to measure voltage by comparing an unknown voltage with a known one. These were used to monitor the displacement at specific locations accurately. The positioning of these potentiometers matches these of the accelerometers discussed in the previous section. Potentiometers measure displacements based on the rotations of the coil around which the wire is wound.

The capacity of the potentiometers was determined based on the expected displacement during the test phase. Measurements are taken through the coil rotations withing the instruments.

Long-stroke potentiometers, specifically 1000 mm, were used in the upper area of the test façade where greater displacements are foreseen. These are indicated by numbers 20, 21 and 22 on Figure 70. The remaining potentiometers, shown in this figure, have a stroke length of 250 mm, which is suitable for the locations where they are installed.

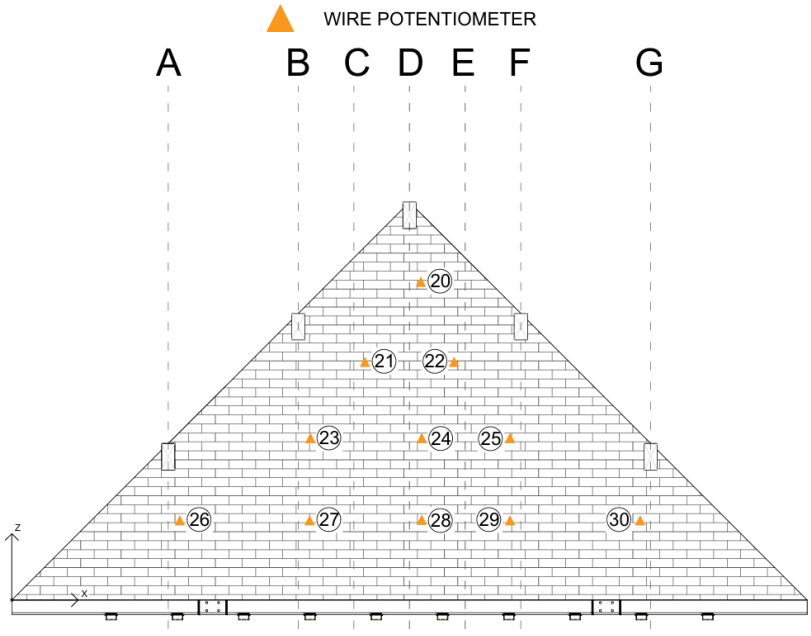

Figure 70 : Schematic overview of the wire potentiometer placed on the gable

Most potentiometers were attached to a structure positioned behind the façade. This structure, specifically designed for supporting these instruments, serves as a reference point for measuring displacement. It was required that this structure had sufficient stiffness to avoid deformation during testing also this setup was used in previous tests for the same purpose. Certain potentiometers, specifically numbers 23, 24 and 25 as indicated in Figure 71 and Figure 72, were directly attached on the setup itself due to structural obstacles. The relative displacement of the specimen was measured in relation to this setup. By determining the sum of the relative displacements between the setup and the frame, the required absolute displacement was obtained.

Figure 71 : Wire potentiometer measuring the relative displacement of the specimen

Figure 72 : Wire potentiometer on the instrumentation frame

5.1.3 Standard Potentiometer

A potentiometer is a type of sensor employed to measure linear displacement by converting mechanical movement into a hydraulic pressure signal. In this study, hydraulic potentiometers were utilized to measure the OOP displacement between the wooden purlins and the masonry see figure below. Additionally, contact potentiometers were attached in the same spot to capture the perpendicular displacement.

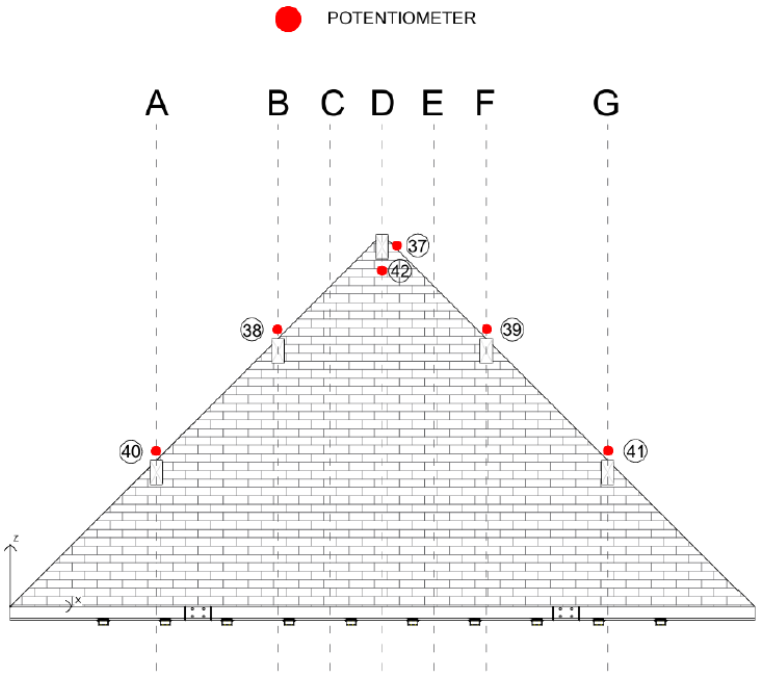

Figure 73 : Schematic overview of the standard potentiometer placed on the gable

5.1.4 Optical acquisition

Reflective spherical markers are strategically positioned at key points on the gable, each coated with a material that reflects infrared light. The setup includes multiple high-speed, high-resolution cameras arranged in different angles from the capture area to record the movement of these markers. Infrared cameras are employed to detect the reflective markers, as they are less influenced by ambient light

conditions. The recorded motion is subsequently analysed to study movement patterns and behaviours. The results of this part are not processed yet thus not included in the paper.

5.2 Definition of vertical loads

To determine the appropriate dimensions of the elements involved in the experimental setup, hypotheses were made regarding realistic values of the vertical loads. A typical surface load for the roof was assumed to be 60 N/m², with a spacing of 1.4 meters between the support beams. Additionally, the self-weight of the timber beam was taken into account, assuming a cross-section of 0.1 m in width, 0.2 m in height, and 6 m in length, with a timber density of 800 N/m³. This results in a self-weight load of 160 N/m

$$q_{roof} = 600\,\frac{N}{m^2} * 1.4m = 840\,\frac{N}{m} \quad [15]$$

$$q_{beam} = 8\,000\,\frac{N}{m^3} * 0.1m * 0.2m * 6m = 160\,\frac{N}{m} \quad [16]$$

By combining these loads and considering a roof span of 6 meters, a resultant point load of 4 kN is calculated to act on the masonry, as illustrated in Figure 74. Due to the eccentricity of the force, the spring must exert twice this force on the gable. Therefore, in this specific case, the required force is 8 kN.

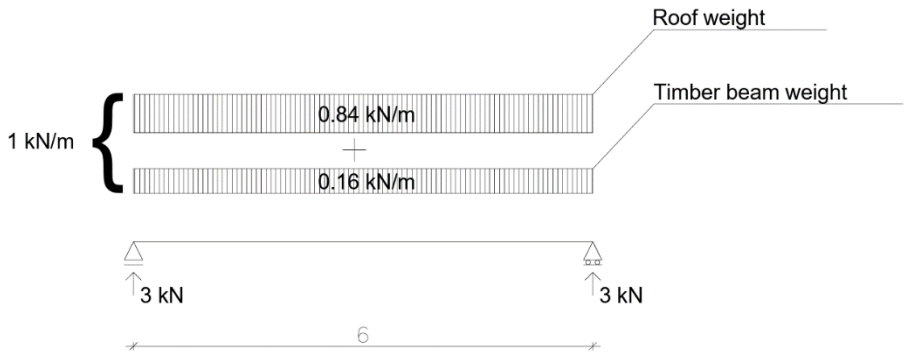

Figure 74 : Schematic overview of the applied loads

Ultimately during the tests, there was an applied load from only 4 kN on the gable and an applied load of 8 kN on the springs.

6 Virtual work method (VWM) - 1

The Virtual Work Method (VWM), also known as the Virtual Work Principal, is employed as a tool in structural mechanics. It is particularly useful for analysing both complex and simple structures, as well as determining the moment capacity of walls and other structural elements. This method is frequently used for calculating deflections and internal force determinations within structures. It involves the use of moments occurring withing construction, along with their corresponding rotation angles. This method is based on the principle of virtual work, which states that the sum of the virtual work done by internal forces during a virtual displacement of the structure is equal to the work done by external forces. This can be expressed by the equation shown in Eq. 15.

$$\sum M_i \cdot \theta_i = V \cdot w_c \qquad [15]$$

Where M_i = the internal moment or bending moment at a particular section of the structure [Nm];
θ_i = the virtual rotation or angular displacement corresponding to the moment M_i [rad];
V = displaced volume [m³];
w_c = load capacity of the wall [kPa].

On the one hand, the internal forces are represented by the occurring bending moments multiplied by the internal virtual displacements or rotations. On the other hand, the external forces are obtained by multiplying the external forces by the actual displacements or rotations of the structure.

6.1 Predicted cracking virtual method

A prediction was made regarding the facades to be tested using the virtual work method, where a hypothesis of the crack pattern was made. Figure 75 and Figure 76 illustrate the expected crack pattern both for line and stepped failure, showing cracks forming due to horizontal and vertical bending moments which provide diagonal cracks in the façade. This phenomenon is provided out of two-way-bending out of plane behaviour. The virtual method assumes that the cracks occur simultaneously. The formula used, comes from the design code for masonry structures AS 3700 [21].

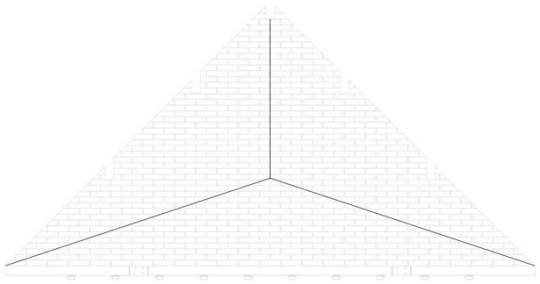

Figure 75 : : Line failure starting on 1/3rd height

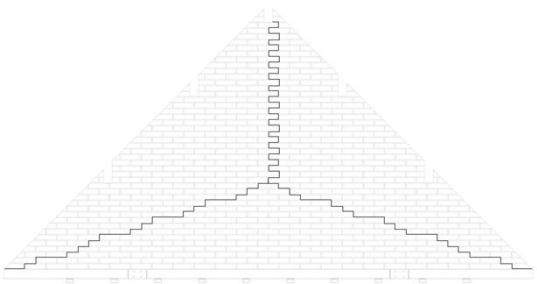

Figure 76 Expected cracking pattern - Stepped failure starting on 1/3rd height

6.1.1 Horizontal and diagonal bending moment capacity

The horizontal bending design capacity based on the moment of resistance of the gable was determined using the following formula:

$$M_h = lesser\ of \begin{cases} \frac{\phi}{2(h_u+t_j)}\left[(f_{ut} - v \cdot f_d) h_u \frac{{t_u}^2}{6}\right] & (weak\ unit\ -\ strong\ joint) \\ \frac{\phi}{h_u+t_j}\left[\tau_u \cdot k_b \frac{(l_u+t_j)}{2} {t_u}^2\right] & (strong\ unit\ -\ weak\ joint) \end{cases} \quad [16]$$

$$\tau_u = f_{v0} + \mu \cdot f_d \qquad (following\ Sharma) \quad [17]$$

Where eq. 16 represents the horizontal bending calculation used for line failure and eq. 17 respectively used for stepped failure. For this research, stepped failure mechanism is expected, after calculations the results show that stepped failure will occur and this equation will be further used, shown in Table 10. To determine the torsional shear stress, the formula of Willis has been used equal to eq. 17. The mean compressive stress was derived at 1/2nd height due to self-weight.

The diagonal bending design capacity based on the moment of resistance of the gable was calculated using the following formula:

$$M_d = \frac{sin\theta}{h_u+t_j}\left[(sin\theta)^3 \tau_u k_b 0.5\left(l_u + t_j\right) \cdot {t_u}^2 + (cos\theta)^3 (f_{mt} + \sigma) \frac{0.5\left(l_u+t_j\right) \cdot {t_u}^2}{6}\right] \quad [18]$$

$$G = \frac{2(h_u+t_j)}{l_u+t_j} = tan\theta \quad [19]$$

Table 10 : Bending moment capacity characteristics

Bending moment capacity characteristics			
Length of one brick	h_u	55	mm
Height of one brick	l_u	230	mm
Thickness of the brick	t_u	105	mm
Thickness of the mortar joint	t_j	10	mm
Tensile strength of bricks	f_{ut}	10	MPa
Torsional shear stress capacity	τ_u	0.84	MPa
Numerical constant (Sharma)	k_b	0.208	[-]
The vertical normal stress	f_d	0.029	MPa
Poisson coefficient	v	0.2	[-]
Coefficient	ϕ	1	[-]
flexural tensile strength of masonry obtained from the bond wrench test	f_{mt}	0.1	MPa
Angle of assumed crack line	θ	0.32	rad

Table 11 : Horizontal and diagonal bending capacity results

Horizontal bending capacity – Line failure	7.77	kNm/m
Horizontal bending capacity – Stepped failure	0.89	kNm/m
Diagonal bending capacity	0.15	kNm/m

6.1.2 Design capacity of the wall

The design capacity of the wall represents the maximum force or load the wall can resist safely without failure, following the design and specifications that was established during the design process. This capacity is closely related to two-way bending and is calculated to indicate the point at which the material begins to degrade or compromise its structure integrity due to the formation of cracks. In the current study, predictions of the peak strength of the walls were revisited using various approaches, consistent with the methods adopted in the study by Graziotti. [20] All methods utilized the codified version of the virtual work method as outlined in the Australian Standard for Masonry Structures (AS 3700) [21], which calculates the peak strength of unreinforced masonry (URM) walls in out-of-plane (OOP) two-way bending according to equation 20.

Once the horizontal and the diagonal bending moments are known, the design capacity of the wall can be calculated.

$$w_c = \frac{2a_f}{{L_d}^2}(k_1 M_h + k_2 M_d) \qquad [20]$$

$$a_f = \frac{1}{1-a/3} \qquad [21] \qquad \text{and} \qquad a = \frac{GL_d}{H_d} \qquad [22]$$

Where a_f = aspect factor;
k_1, k_2 = the coefficients for out-of-plane lateral resistance;
M_h = horizontal bending capacity [kNm];
M_d = diagonal bending capacity [kNm];
L_d = the design length of the specimen [m].

The slope factor was calculated following Eq. 19 and will be further used for the association of k_1 and k_2. The coefficients R_{f1} and R_{f2} are restraint factors, related to the supported edges of the wall. These factors are equal to 0 if there is no rotational restraint, to 1 if the edge is completely fixed and prevents rotation and to intermediate values for partial rotational restraint. The used method to calculate the PCR has been validated against experimental studies, as detailed in references [20] [22]. These studies demonstrate good results when using a value of 0.5, which is recommended for performing the assessment. The subsequential factors k_1 and k_2 were calculated following Table 12 for α greater than 1 and both vertical edges supported.

Table 12 : Coefficients for out-of-plane lateral load resistance

TABLE 7.5
COEFFICIENTS FOR OUT-OF-PLANE LATERAL LOAD RESISTANCE

Opening	Number of vertical edges supported	Slope factor α	Aspect factor ($\alpha\alpha$)	k_1	k_2
No	Both	≤1	$\frac{1}{\left(1-\frac{\alpha}{3}\right)}$	$\frac{R_{f1}+R_{f2}}{2}+1-\alpha$	$\alpha\left(1+\frac{1}{G^2}\right)$
No	Both	>1	$\frac{\alpha}{\left(1-\frac{1}{3\alpha}\right)}$	$\frac{R_{f1}+R_{f2}}{2}$	$1+\frac{1}{G^2}$
No	One	≤1	$\frac{1}{\left(1-\frac{\alpha}{3}\right)}$	R_n	$\alpha\left(1+\frac{1}{G^2}\right)$
No	One	>1	$\frac{\alpha}{\left(1-\frac{1}{3\alpha}\right)}$	R_n	$1+\frac{1}{G^2}$
Yes	Both	≤1	$\frac{1}{\left(1-\frac{\alpha}{3}\right)+\frac{L_o}{L_d}\left(1-\frac{\alpha}{2}\right)}$	R_n	$\alpha\left(1+\frac{1}{G^2}\right)$
Yes	Both	>1	$\frac{\alpha}{\left(1-\frac{1}{3\alpha}\right)+\frac{L_o}{2L_d}}$	R_n	$1+\frac{1}{G^2}$

Table 13 : Design capacity of the wall

Design capacity of the wall	0.35	kPa

6.1.3 Virtual working method (VWM)

There will be assumed that the cracking pattern of the gable wall will be centre pointed around 1/3rd height. The virtual displacement was assumed to be a small, uniform out-of-plane deflection at one-third height in the middle of the gable, corresponding to a unit virtual force.

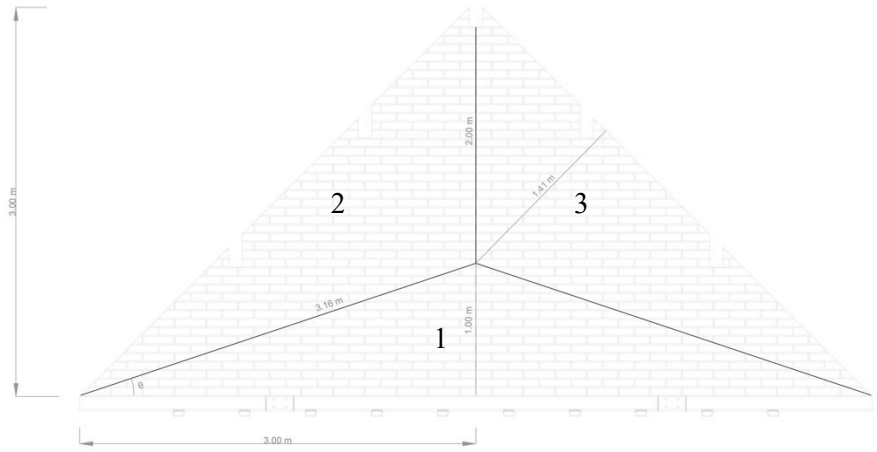

Figure 77 : Design of the predicted cracking pattern at 1/3rd height with their measurements

The internal work was calculated by using the bending moments from previous paragraph with their corresponding rotation angle, while the external work was determined by the virtual force applied at the centre of the gable.

Table 14: Virtual method - prediction

Virtual method (VM) – Hypothesis 1/3rd height			
Angle in plane	θ	0.32	rad
Displacement	Δ'	1.00	mm
Displaced volume – triangle 1	V_1	1.00	m^3
Displaced volume – triangle 2	V_2	1.00	m^3
Displaced volume – triangle 3	V_3	1.00	m^3
Total displaced volume	$\boldsymbol{V_{tot}}$	3.00	m^3
Rotation angle corresponding to M_h	θ_h	1.00	rad
Rotation angle corresponding to M_d	θ_d	1.58	rad

For the calculation of the internal work, the bending moments are multiplied by their corresponding internal rotation angles as well as by the associated length over which the moment acts. Next, this is equated to the total deformed displacement volume multiplied by the design capacity of the wall, as shown in Eq. 23. Subsequently, the design capacity can be calculated and compared to the results of the used formulas provided in the previous paragraph.

$$\sum M_i \cdot \theta_i = V_{tot} \cdot w_c \qquad [23]$$

$$1 \cdot M_h \cdot \theta_h + 2 \cdot M_d \cdot \theta_d = V_{tot} \cdot w$$

Table 13: Design capacity of the wall using VWM

Design capacity of the wall (VWM)	1.20	kPa

7 Test results OOP shaking on gable walls

The results of the full-scale dynamic experiments are presented and discussed in terms of the fundamental vibration modes of the gable walls; photographs documenting the progression of damage in the walls during the incremental dynamic test series; failure mechanisms and how these relate to expected mechanisms according to the anticipated boundary conditions found in literature; and the IDT curves which represent the Incremental Dynamic Tests. The same set of damage states used to present the results in Graziotti et al [1]. is reused here, as shown in Figure 48. This was a preliminary assignment of damage states, these classifications may change in the future as the results are further analysed and elaborated. DS1 corresponds to no visible structural damage, DS2 to light structural damage, DS3 to moderate damage with full development of the collapse mechanism, DS4 to severe damage with negligible residual capacity, and finally, DS5 corresponds to very severe damage associated with global or partial collapse of the panel. All three gables were tested up to the DS5 stage.

7.1 Dynamic identification

Dynamic properties, particularly the first natural vibration modes of each tested specimen, were continuously monitored throughout the entire test series. Changes in dynamic properties serve as an indication of damage, which in some cases could be documented through visual observation. The method used to observe the formation of cracks during the test was conducted through hammering. The detailed analysis of the collected data still needs to be performed and will not be fully covered in this thesis.

These tests were conducted between transitions corresponding FM1-10 and FM2-300, or whenever structural damage was detected, depending on whether the facades were subjected to stiff, semi-stiff or flexible testing conditions. FM1 is equivalent to the first period of the masonry gable and the same applies to FM2 but corresponding to the second period. Special attention was paid to the frequency and time period associated with the first and second natural vibration modes of the gables. To identify these natural frequencies, frequency domain decomposition (FDD) was utilized. A numerical model of the gable showed a frequency of with free top edges and fixed bottom edges in their undamaged state. This period aligns with the linear elastic eigenvalue analysis performed using shell FE models developed in MIDAS Gen [19]. Significant increases in the time period related to the first natural mode of vibration were observed in RN tests conducted after cycles where the specimen transitioned between the defined damage states.

7.2 Damage pattern and failure mechanism

This section summarizes the visual observations of damage made for all the full-scale tested specimens during their incremental dynamic test series. All observed damage was classified according to one of the damage states shown in Figure 78. All specimens were subjected to testing up to the damage state 5.

The classification of the damage states is as outlined below [20]:

- DS1 no visible structural damage
- DS2 slight structural damage
- DS3 moderate damage with full development of the collapse mechanism
- DS4 heavy damage with negligible residual capacity and ultimately
- DS5 very heavy damage associated with global or partial collapse

Figure 78 : Visualization of the damage state progression

7.2.1 Gable 1 - Configuration with stiff roof structure

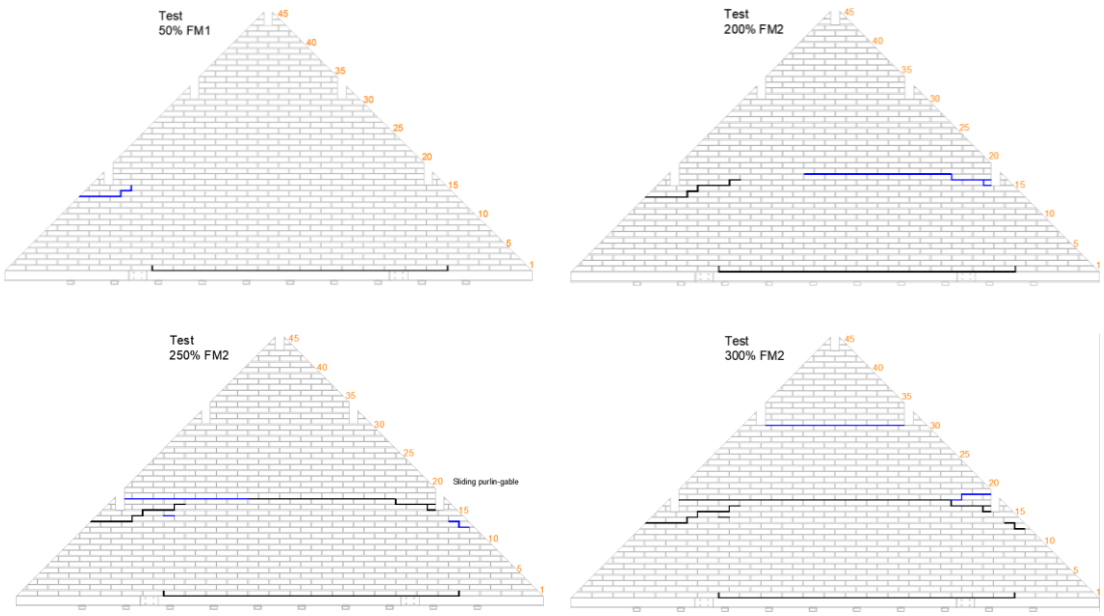

Figure 79 : Evolution of damage & development of specimen collapse mechanism in gable 1

During the initial test at 10% FM1, slight structural damage was observed, marked by the appearance of a horizontal crack along the base of the gable. As the testing intensity increased to 50% FM1, additional damage to the gable was noted. A horizontal crack began to develop beneath one of the lower purlins contact points.

In subsequent tests, ranging from 100% FM2 to 200% FM2, the previously recorded crack propagated laterally from the left side to the right side of the gable. Despite the crack spanning the entire width of the structure, the specimen remained in Damage State 2 (DS2), as the collapse mechanism had not yet fully developed.

DS3 was reached during the test at 250% FM2. At this stage, the previously formed horizontal crack began functioning as a hinge, allowing the top and bottom sections of the gable to move independently. This stage also saw the displacement of the lower right purlin.

The subsequent test at 300% FM2 resulted in further damage, including the formation of an additional crack beneath the top two purlins, this new crack initiated a secondary collapse mechanism, further compromising the integrity of the structure.

Ultimately, the specimen reached DS5 and collapsed during the test at 350% FM2. This final phase of the testing clearly demonstrated the limitations of the structure under progressively increasing accelerations.

7.2.2 Gable 2 - Configuration with semi-stiff roof structure

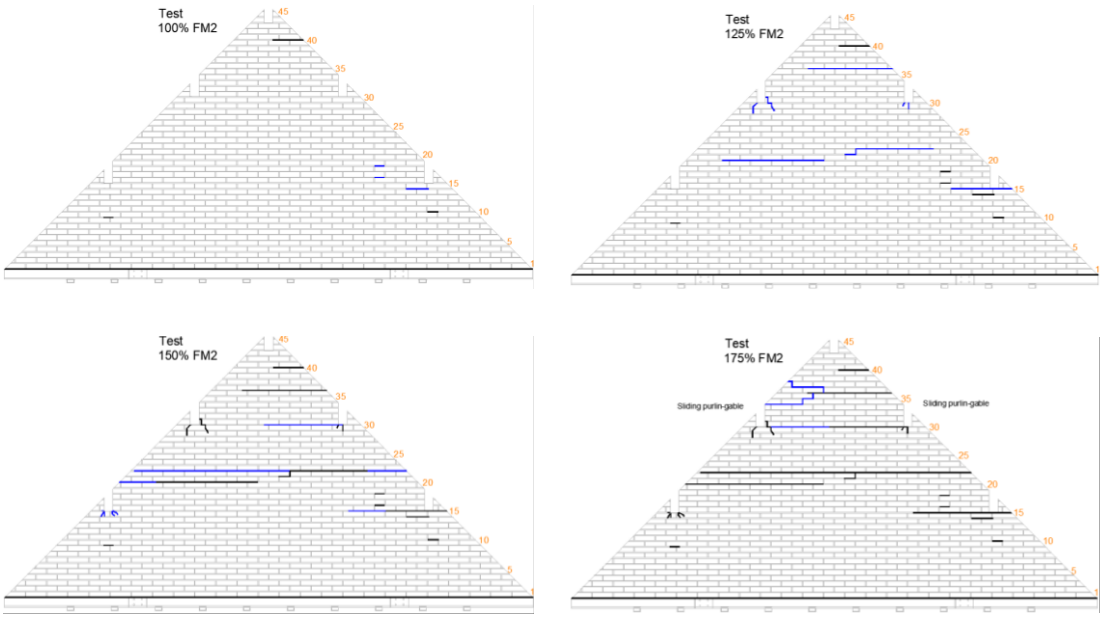

Figure 80 : Evolution of damage & development of specimen collapse mechanism in gable 2

As anticipated, the initial test conducted at 10% FM1 resulted in slight structural damage to Gable 2, which closely mirrored the observations made in Gable 1 under similar conditions. This early damage was characterized by the formation of a horizontal crack along the base of the gable, indicating a preliminary response of the structure to the applied acceleration. Despite this initial indication of stress, no

significant visible damage exceeding one brick length was observed until the testing intensity reached 100% FM1.

The progression of structural damage became more pronounced as the testing advanced to higher g-forces. Notably, crack formation was observed around the support points of the purlins during the tests conducted at 125% FM2 and 150% FM2. These cracks indicated localized stress concentrations. At 150% FM2, the situation escalated as the collapse mechanism began to manifest, leading to the classification of the structure into Damage State 3 (DS3).

The subsequent test at 175% FM2 revealed further developments in the structural instability. It was observed that the purlins, which had previously shown signs of stress, began to slide within the masonry cut-outs. By this point, the mechanism was fully developed, rendering the structure entirely unstable (DS4).

Finally, the testing at 200% FM2 led to a partial collapse of the gable (DS5). This collapse was driven by the extension of the existing horizontal crack, which, in combination with the increased rocking motion of the top portion of the gable, resulted in the structure's failure.

7.2.3 Gable 3 - Configuration with flexible roof structure

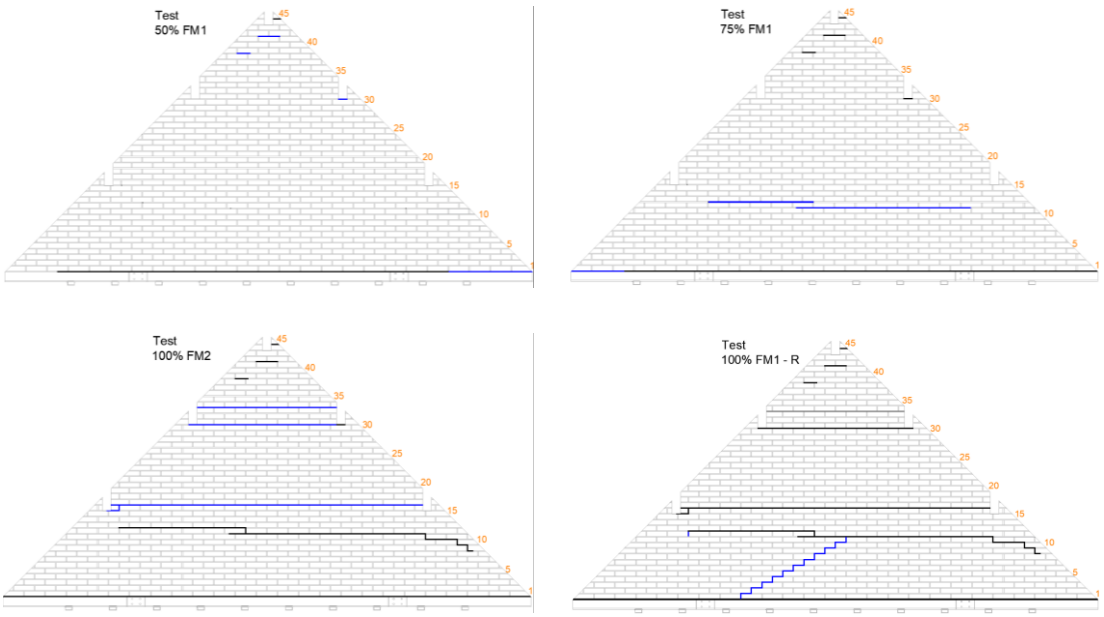

Figure 81 : Evolution of damage & development of specimen collapse mechanism in gable 3

In a manner consistent with the observations made in Gables 1 and 2, the initial test conducted at 10% FM1 on Gable 3 resulted in the formation of a horizontal crack along the base of the structure. This early crack was fully developed by the time the testing intensity reached 75% FM1. Prior to this, small cracks had begun to appear throughout the masonry at 50% FM1.

As testing progressed, the next significant crack emerged at 75% FM1, manifesting as a horizontal crack in the middle of the gable at brick level 11. By the time the testing intensity reached 75% FM2, this horizontal crack had extended further, and the top brick, which had earlier shown signs of cracking, became detached from the wall. This detachment was an indicator of the intensity of the shaking.
Gable 3, characterized by its flexible roof design, remained in DS2 until the testing intensity reached 100% FM2. At this juncture, the gable began to exhibit additional signs of distress as new cracks emerged. Specifically, a horizontal crack at brick level 16 formed above the previously identified crack, while two more horizontal cracks developed at brick levels 30 and 33, situated between the top purlin lay-ins.

By this stage, the gable had become unstable, prompting a transition into DS3. The observed extent of movement and the cumulative damage suggested that the gable might have been on the verge of advancing into DS4. To better understand the gable's capacity to remain upright despite the significant damage, the testing intensity was temporarily reduced to 100% FM1-R. This reduction served as an assessment tool, gauging whether the gable could withstand lower stress levels after having already sustained considerable damage. Although the gable did not progress to DS5 at this point, a diagonal crack was observed to extend from the initial base crack to the lower horizontal crack at brick level 11.
Gable 3 ultimately reached DS5 upon resumption of testing at 125% FM2, resulting in the partial collapse of the wall. This collapse was characterized by the failure of all structural elements above brick level 16.

7.3 Data analysis

After conducting the tests on the facades, the data were analysed to gain a better understanding of the structure’s behaviour under the applied acceleration inputs. This data is presented in appendices B and C. Only the first two facades were considered, as the data for the third gable had not yet been processed at the time of writing this thesis.

The graphs below show the IDT curves, which stand for Incremental Dynamic Testing. These curves assist in understanding how a structure respond to varying levels of seismic intensity and can be used to assess the seismic capacity and vulnerability of the structure. The measured acceleration along the wall height was normalized with the peak table acceleration (PTA) with the difference between the top table, the bottom table and the ridge structure acceleration. The acceleration profiles are presented for the façade exposed to out-of-plane loading.

Figure 82 presents the peak table acceleration curves as a function of central deflection for the first gable tested under the stiff roof configuration. On the y-axis, the applied acceleration is plotted, representing the imposed load, while the x-axis shows the gable's response in terms of displacement. These curves illustrate

the gable's capacity to withstand seismic loads. In the first test, identical input motions were applied to both the top and bottom tables, which explains the similarity between the two curves as well as the ridge acceleration curve.

At the start of the test, there is a sharp increase as the PTA rises. This is followed by a plateau where central displacement continues to increase steadily. Finally, the PTA value stabilizes around a constant level while the displacement significantly increases, reaching a maximum of 42.16 mm for the top table.

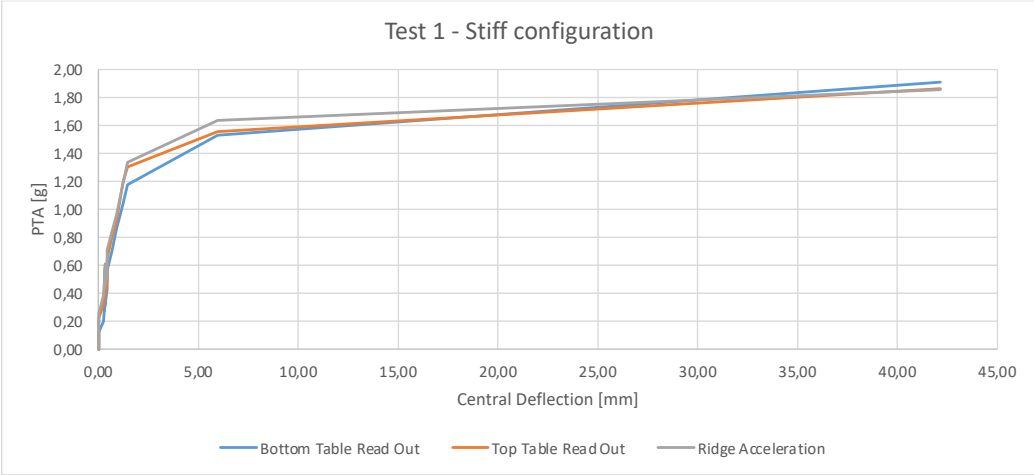

Figure 82 : IDT curve Test 1, stiff configuration - Central deflection-PTA curve of the bottom-, top table and ridge acceleration

The same applies to Figure 83, where the PTA is shown as a function of relative displacement. Here, a significant increase can be observed, following an almost linear trend. A slight drop occurs around a displacement of 10 mm. Similar to the previous figure, the three curves are nearly identical for the same reasons.

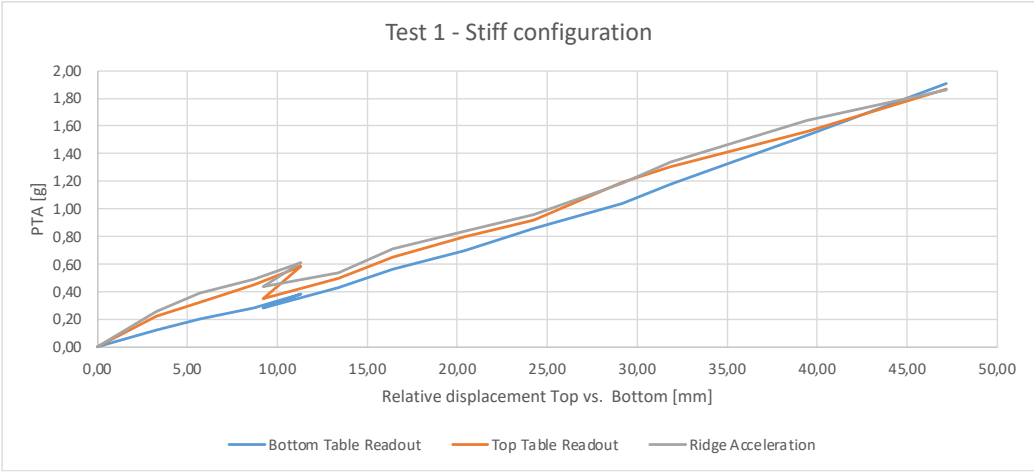

Figure 83 : IDT curve Test 1, stiff configuration – Relative displacement Top vs. Bottom-PTA curve of the bottom-, top table and ridge acceleration

Figure 84 illustrates the same relationship as Figure 82, but it pertains to test 2. In this test, the same motion was applied to the bottom table, while a different input was used for the top table. The curve initially shows an upward slope, reaching a peak before dropping back down. It then continues to align with the bottom line and the ridge acceleration curve.

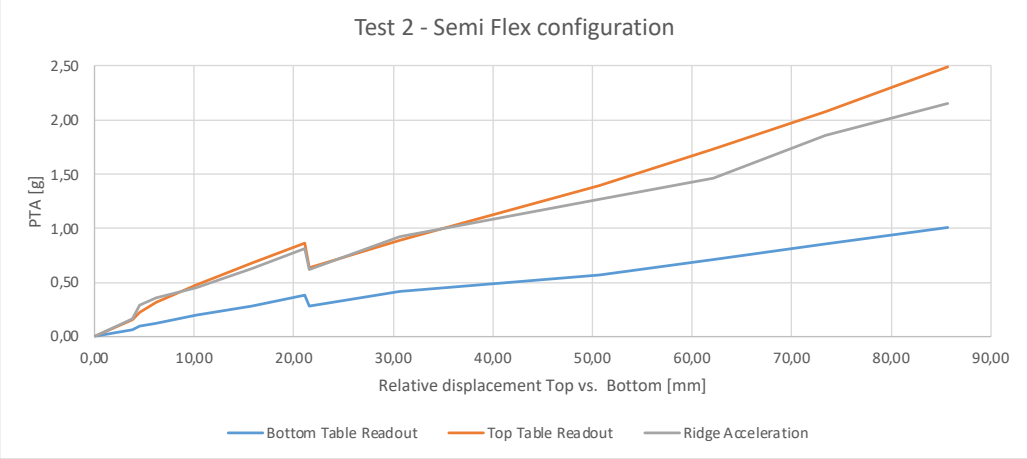

Figure 84 : IDT curve Test 2, semi-flex configuration - Central deflection-PTA curve of the bottom-, top table and ridge acceleration

Figure 85 illustrates the same trend as Figure 83, but refers to test 2. It shows similar increasing curves, with higher values for the top and stiff acceleration at the same deflection. Although a drop is also observed, it is less pronounced compared to the one from the first test.

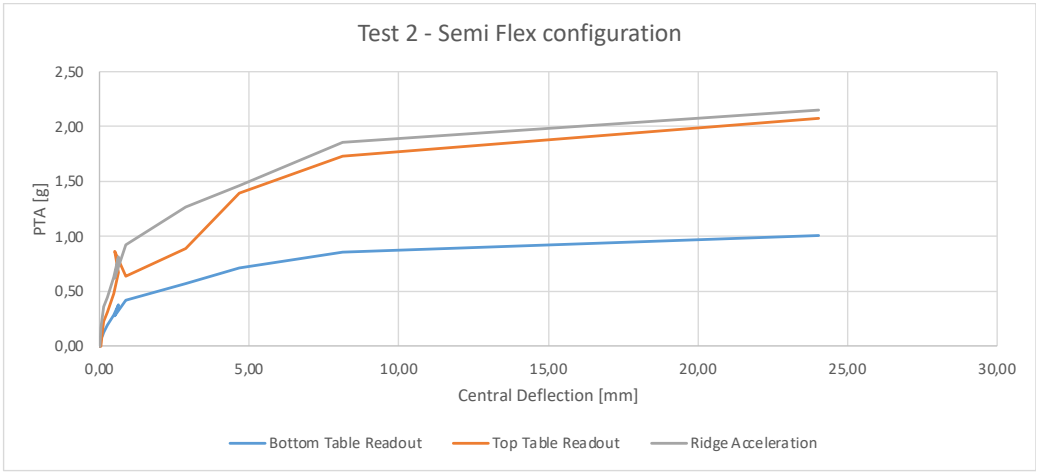

Figure 85 : IDT curve Test 2, semi-flex configuration – Relative displacement Top vs. Bottom-PTA curve of the bottom-, top table and ridge acceleration

Finally, the results of the two tests have been combined to provide a comparative overview, as shown in Figure 86 and Figure 87. Figure 87 compares the IDT for central displacement, with the blue curve representing the results from the first test (the stiff configuration) and the orange curve representing the second test (the semi-flex configuration). It is observed that the top table in the second test experiences higher acceleration but is associated with a smaller displacement. In contrast,

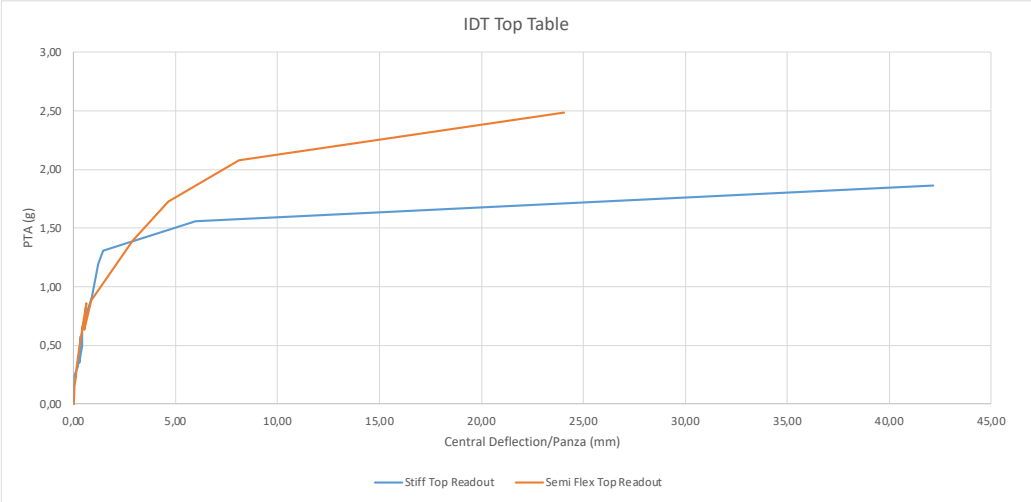

Figure 86 : IDT curve comparison between test 1 (stiff configuration) and test 2 (semi-flex configuration) – Central deflection-PTA curve of the top table

Figure 87 shows that the second test results in a lower PTA for the bottom table compared to the first test. Both curves exhibit a similar shape, as predicted. It is also noted that the maximum deflection in the first test is greater than that in the second test. These values can be found in appendices B and C.

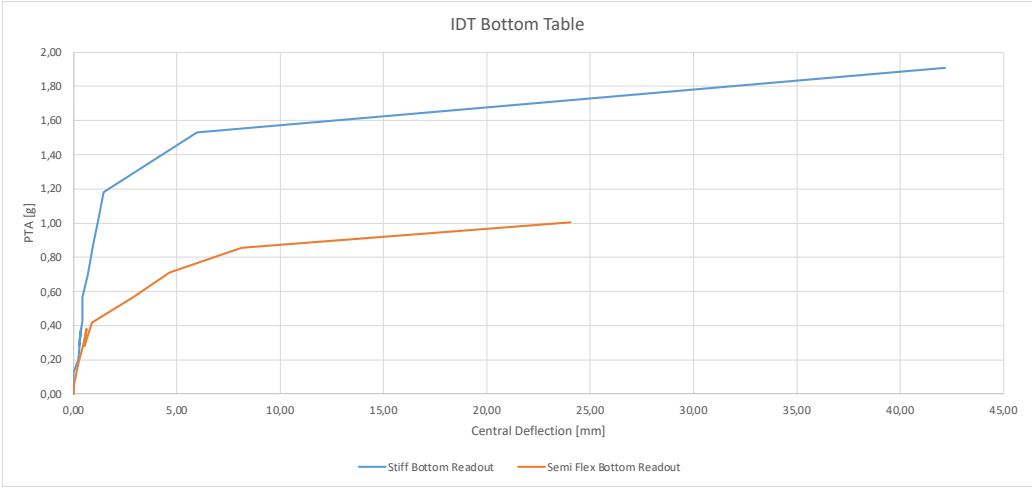

Figure 87 : IDT curve comparison between test 1 (stiff configuration) and test 2 (semi-flex configuration) – Central deflection-PTA curve of the bottom table

8 Virtual work method (VWM) - 2

8.1 Virtual method after the test

The experiments revealed that the expected diagonal crack pattern did not occur, instead, horizontal cracks developed. These originate from vertical bending moments. Multiple cracks appeared during the test but the principle of the VWM assumes that the cracks occur simultaneously. For this reason, the first significant crack is used for analysis. This crack caused damage that exceeded the wall's resistance, illustrated in Figure 88.

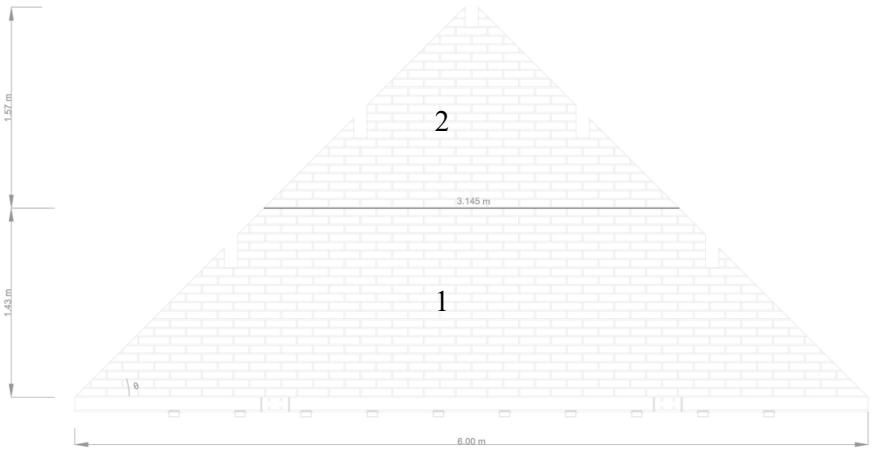

Figure 88 : Post test cracking pattern – Horizontal line failure

After completing the experimental phase, it became clear that the predictions were inaccurate, a new calculation is required based on a different crack pattern. Additionally, the assumption for certain parameters can be replaced with the actual values obtained from the characterization tests. These new calculations will focus on one-way bending out-of-plane instead of the previously used two-way bending approach.

8.1.1 Vertical bending moment capacity

The vertical bending design capacity based on the moment of resistance of the gable was determined using the following formula:

$$M_{cv} = \phi \cdot k_{mt} \cdot f'_{mt} \cdot Z_d + f_d \cdot Z_d \leq 0.3 \cdot \phi \cdot k_{mt} \cdot f'_{mt} \cdot Z_d \qquad [24]$$

Where ϕ = strength reduction factor, 0.6 for bending;
k_{mt} = a coefficient related to the material properties or configuration, 1.0 for other than AAC masonry;

f'_{mt} = characteristic flexural tensile strength of masonry [MPa];
Z_d = section modulus of the bedded area [mm³];
f_d = mean compressive stress acing on the bed joint due to vertical load [MPa].

Table 14 : Bending moment capacity characterization from tests

Bending moment capacity characteristics			
Section modulus	Z_d	1.84 10^6	mm³
The mean compressive stress	f_d	0.029	MPa
Coefficient	k_{mt}	1.0	[-]
Strength reduction factor	ϕ	0.6	[-]
flexural tensile strength of masonry obtained from the bond wrench test	f_{mt}	0.21	MPa

8.1.2 Virtual working method (VWM)

The internal work was calculated by using the bending moment from previous paragraph with the corresponding rotation angle, while the external work was determined by the virtual force applied at the centre of the gable.

Table 14: Virtual method - prediction

Virtual method (VM) – Hypothesis 1/3rd height			
Displacement	Δ'	1.00	mm
Displaced volume – trapezium (1)	V_1	2.93	m³
Displaced volume – triangle (2)	V_2	0.35	m³
Total displaced volume	$\boldsymbol{V_{tot}}$	3.28	m³
Rotation angle corresponding to M_v	θ_v	0.69	rad

For the calculation of the internal work, the bending moment is multiplied by its corresponding internal rotation angle and the length over which the moment acts. This product is then equated to the total deformed displacement volume, multiplied by the design capacity of the wall, as illustrated in Eq. 23. Subsequently, the design capacity can be calculated and compared to the results obtained from the formulas presented in the preceding paragraph.

$$\sum M_i \cdot \theta_i = V_{tot} \cdot w_c \qquad [25]$$

$$1 \cdot M_v \cdot \theta_h = V_{tot} \cdot w$$

9 Conclusion

Based on findings during the study the following conclusion can be drawn.

9.1 Conclusion DIC

DIC provides a more comprehensive understanding of the entire specimen compared to traditional methods such as potentiometers. While potentiometers measure the relative displacement at predetermined points, they do not offer visualization of cracks or other damage that may occur in the material. In contrast, DIC enables detailed observation of crack development and propagation throughout the specimen, making it a valuable alternative or addition to potentiometers. However, during the testing of other triplet specimens, issues arose with various recording methods and maintaining proper focus, which affected the accuracy and consistency of the data collected. The camera calibration needs to be optimized.

The use of potentiometers has proven to be a reliable method for collecting predictable and accurate data in the laboratory. The data obtained through this method clearly demonstrate that the shear stress graph aligns well with the graph of the increasing force, while the normal stress and horizontal force graphs are consistent with expected outcomes.

In comparison, the Digital Image Correlation (DIC) data were analysed alongside the potentiometer data to assess the viability of DIC as an alternative measurement technique. The analysis revealed that the values obtained through the DIC method closely corresponded to those recorded by the potentiometers. This close correlation suggests that the DIC system has significant potential as a replacement for potentiometers in similar experimental setups.

9.2 Conclusion damage states

It was observed that the development of the failure mechanisms exhibited consistent patterns across the three gables. In each tested gable, the initial cracking observed was characterized by a horizontal crack situated at the base. Additionally, the failure mechanism was characterized by the formation of a horizontal crack between the purlin contact points. This pattern of crack development suggests that the structural response was primarily governed by one-way bending, rather than the two-way bending that had been initially predicted.

9.3 Conclusion virtual working method (VWM)

The predicted crack pattern derived using the Virtual Work Method (VWM) did not align with the actual crack pattern observed during the physical testing of the gable. The real-life crack pattern demonstrated characteristics more consistent with one-way bending rather than the two-way bending mechanism that the original VWM prediction assumed. In light of this observation, a revised VWM analysis needs to be conducted, incorporating data from the material characterization tests and assuming a one-way bending behaviour of the wall. This recalibration aimed to achieve a more accurate representation of the gable's structural response under the tested conditions.

Further research in this area could involve the development of a virtual work method for one-way bending that integrates data obtained from characterization tests and closely mirrors the crack patterns observed during the shake table tests. It is important to note that this project is still ongoing at the EUcentre, where they are actively processing all the collected data. These experimental findings will serve as crucial benchmarks for refining existing numerical models and for the creation of new analytical tools, including those based on single-degree-of-freedom systems, thereby advancing the field of structural seismic analysis. In addition, optical acquisition techniques are being developed for this project, which could offer a more detailed understanding of crack development and the stability of the gable during dynamic testing.

References

[1] "EN 1015-11 "Methods of test for mortar for masonry - Part 11: Determination of flexural and compressive strength of hardened mortar"," European Committee for Standardization, Brussels, 1999.

[2] "EN 772-1 "Methods of test for masonry units - Part 1: Determination of compressive strength"," European Committee for Standardization, Brussels, 2011.

[3] "EN 6790," European Standard, 2005.

[4] "EN 1052-3 "Methods of Test for Masonry - Part 3: Determination of Initial Shear Strength"," European Committee for Standardization, Brussels, 1998.

[5] "EN 1052-5 "Methods of Test for Masonry - Part 5: Determination of Bond Strength by the Bond Wrench Method"," European Committee for Standardization, Brussels, 1998.

[6] S. Sharma, U. Tomassetti, L. Grotto and F. Graziotti, "Out-of-plane two-way bending shaking table tests on single leaf and cavity walls," EUCENTRE Foundation, Pavia, 2018.

[7] *EN 1052-1 "Testing of masonry - Part 1: Determination of compressive strength",* Brussels: European Committee for Standardization, 1998.

[8] "EN 1052-3/A1 "Methods of test for masonry – Part 3: Determination of compressive strength"," European Committee for Standardization, Brussels, 2007.

[9] "EN 1052-3 "Methods of test for masonry - Part 3: Determination of initial shear strength"," European Committee for Standardization, Brussels, 2002.

[10] ZEISS Quality Software, *ZEISS Insppect Corralte,* ZEISS, 2023.

[11] Y. T. a. M. M. M. A. Hossain, "Application of digital image correlation (DIC) technique for semi interlocking masonry (SIM) panels under large cyclic in-plane shear displacement," 2021.

[12] M. K. Howlader, "In-Plane Behaviour of Unreinforced Masonry (URM) Walls with Openings in Australian Heritage Construction," University of Newcastle, Newcastle, 2020.

[13] K. Q. H. X. a. A. A. B. Pan, "Two-dimensional digital image correlation for in-plane displacement and strain measurement: a review," Meas. Sci. Technol, 2009.

[14] Correlated-Solutions, "Vic-2D Digital Image Correlation Version 6 Testing Guide," Correlated-Solutions, 2014.

[15] ZEISS Quality Suite, *ZEISS Quality Tech Guide,* 2023.

[16] F. M. a. M. A. S. R. Ghorbani, "Full-field deformation measurement and crack mapping on confined masonry walls using digital image correlation," Exp. Mech., vol. 55, no. 2, 2015.

[17] S. S. F. M. Michele Mirra, “Input signals for out-of-plane seismic testing of masonry gables,” Delft Univeristy of Technology (TUDelft), Delft, 2024.

[18] *EN 1993-1-8 "Design of Steel Structures : Design of Joints",* Brussels: European Committee for Standardization, 1993.

[19] *midas gen,* MIDAS Information Technology Co., 2018.

[20] F. Graziotti, U. Tomassetti, S. Sharma, L. Grottoli and G. Grottoli, “Experimental response of URM single leaf and cavity walls in OOP two-way bending generated by seismic excitation,” EUCENTRE, Pavia, Italy, 2019.

[21] “AS 3700-2001 "Masonry Structures",” Australian Standard, Sydney, Australia, 2001.

[22] U. T. L. G. a. F. G. S. Sharma, “Two-way bending experimental response of URM walls subjected to combined horizontal and vertical seismic excitation vol. 219,” Eng. Struct, 2020.

Appendices

Appendix A

HEB300 welded plates	
Grade	8.8
Bolt	M24
N_{fp}	2
A	353 mm2
F_{tb}	800 MPa
Preloading force	
γ_{M7}	1.1
$F_{p,Cd}$	180 KN
Slip resistance	
γ_{M3}	1.25
μ	0.3
F_{Rd}	86 kN
Total slip resistance	
#n bolts	9
$F_{tot,Rd}$	86 kN
Resistance	
F_b	667 kN

Appendix B

Stiff

				Accelerations (g)					Displacements (mm)					
Test #	Scaling Fact	Motion	Force (kN)	Ridge	Top Table Ri	Bottom Tab	Avg Top+Bo	Shake Table	Ridge Beam	Central Defl	Centre Rigic	Top Table Ri	Bottom Tab	Rel Disp Top vs. Bottom
1	0		0,00	0,00	0,00	0,00	0,00	0,00	0,00	0,00	0,00	0,00	0,00	0,00
2	30	FM1	3,91	0,26	0,22	0,12	0,17	0,12	1,53	0,00	0,00	10,65	8,01	3,29
3	50	FM1	5,45	0,39	0,32	0,20	0,26	0,19	4,60	0,22	0,22	17,73	15,28	5,70
4	75	FM1	7,14	0,49	0,45	0,28	0,37	0,28	6,78	0,28	0,28	26,17	22,72	8,69
5	100	FM1	8,73	0,61	0,58	0,38	0,48	0,37	8,69	0,35	0,35	34,41	30,04	11,30
6	50	FM2	6,70	0,44	0,35	0,28	0,32	0,29	7,09	0,27	0,27	23,39	21,75	9,18
7	75	FM2	9,91	0,53	0,49	0,43	0,46	0,43	10,53	0,41	0,41	34,52	32,38	13,42
8	100	FM2	11,65	0,71	0,65	0,56	0,61	0,57	12,74	0,43	0,43	45,92	42,14	16,41
9	125	FM2	13,15	0,84	0,80	0,70	0,75	0,69	15,87	0,68	0,68	57,09	52,20	20,40
10	150	FM2	15,38	0,96	0,92	0,86	0,89	0,86	19,29	0,91	0,91	68,28	61,68	24,23
11	175	FM2	18,45	1,19	1,19	1,04	1,12	1,03	23,04	1,21	1,21	82,11	74,59	29,17
12	200	FM2	20,91	1,34	1,31	1,18	1,25	1,17	25,38	1,45	1,45	93,71	84,02	31,85
13	250	FM2	27,25	1,64	1,56	1,53	1,54	1,51	31,32	5,97	5,97	117,67	104,56	39,45
14	300	FM2	26,81	1,86	1,87	1,91	1,89	1,88	36,71	42,16	42,16	141,07	124,61	47,19
15	350	FM2												

Appendix C

Semi Flex

				Accelerations (g)					Displacements (mm)					
Test #	Scaling Fact	Motion	Force (kN)	Ridge	Top Table Ri	Bottom Tab	Shake Table		Ridge Beam	Central Defl	Centre Rigic	Top Table Ri	Bottom Tab	Rel Disp Top vs. Bottom
1	0		0,00	0,00	0,00	0,00	0,00		0,00	0,00	0,00	0,00	0,00	0,00
2	10	FM1	1,83	0,16	0,16	0,07	0,05		2,04	0,03	0,03	3,59	5,84	3,77
3	20	FM1	3,66	0,29	0,22	0,10	0,09		3,83	0,10	0,10	6,56	8,86	4,49
4	30	FM1	4,92	0,36	0,31	0,12	0,12		6,01	0,14	0,14	10,19	13,72	6,21
5	50	FM1	6,90	0,45	0,48	0,19	0,20		9,90	0,27	0,27	16,71	23,91	10,23
6	75	FM1	8,01	0,62	0,67	0,28	0,28		14,29	0,46	0,46	24,75	36,68	15,75
7	100	FM1	9,75	0,81	0,86	0,38	0,38		18,48	0,62	0,62	32,72	49,36	21,12
8	50	FM2	8,85	0,62	0,63	0,28	0,28		15,57	0,52	0,52	23,31	39,65	21,56
9	75	FM2	11,56	0,93	0,89	0,42	0,42		22,92	0,88	0,88	34,28	58,71	30,58
10	100	FM2	15,20	1,26	1,39	0,57	0,57		39,71	2,89	2,89	47,16	92,26	50,72
11	125	FM2	17,22	1,46	1,73	0,71	0,71		48,81	4,66	4,66	58,61	115,06	62,13
12	150	FM2	20,00	1,86	2,08	0,86	0,86		58,47	8,13	8,13	69,88	137,21	73,45
13	175	FM2	27,16	2,15	2,49	1,00	1,00		69,19	24,05	24,05	82,01	160,95	85,68
14	200	FM2												